

1  
2  
3  
4  
5  
6  
7  
8  
9  
10  
11  
12  
13  
14  
15  
16  
17  
18  
19  
20  
21  
22

**Deep Learning Driven Simulations of Boundary Layer Clouds over the Southern  
Great Plains**

Tianning Su<sup>1\*</sup>, Yunyan Zhang<sup>1</sup>

<sup>1</sup>Lawrence Livermore National Laboratory, Livermore, CA, USA

Submission to *Geoscientific Model Development*

\*Corresponding authors: [su10@llnl.gov](mailto:su10@llnl.gov)

23 **Abstract.** Based on long-term observations at the Southern Great Plains site by the  
24 Atmospheric Radiation Measurement (ARM) program for training and validation, a  
25 deep learning model is developed to simulate the daytime evolution of boundary-layer  
26 clouds (BLCs) from the perspective of land-atmosphere coupling. The model takes  
27 ARM measurements as inputs including early-morning soundings and the diurnal-  
28 varying surface meteorological conditions and heat fluxes and predicts hourly estimates  
29 as outputs including the determination of cloud occurrence, the positions of cloud  
30 boundaries, and the vertical profile of cloud fraction. The deep learning model offers a  
31 good agreement with the observed cloud fields, especially on the accuracy in  
32 reproducing cloud occurrence and base height. If substituting the inputs by reanalysis  
33 data from ERA5 and MERRA-2, the outputs of the deep learning model provide a better  
34 agreement with observation than the cloud fields extracted from ERA5 and MERRA-2  
35 themselves. From such practice, the deep learning model shows great potential to serve  
36 as a diagnostic tool on the performance of physics-based models in simulating  
37 stratiform and cumulus clouds. By quantifying biases in clouds and attributing them to  
38 the simulated atmospheric state variables versus the model parameterized cloud  
39 processes, this observation-based deep learning model may offer insights on the  
40 directions to improve the simulation of BLCs in physics-based models for weather  
41 forecasting and climate prediction.

42

## 43 **1 Introduction**

44 Boundary layer clouds (BLCs), comprising primarily of stratiform and shallow  
45 cumuli, exert a profound influence on the Earth's radiative balance (Betts, 2009;  
46 Teixeira and Hogan, 2002; Lu et al., 2013; Golaz et al., 2002). Their formation and  
47 evolution are critically shaped by the interactions between surface, planetary boundary  
48 layer (PBL) and free troposphere (Miao et al., 2019; Berg and Kassianov, 2008; Zhang  
49 and Klein, 2013; Guo et al., 2017, 2019; Zhang et al., 2017). Numerous studies  
50 investigated the controlling factors of BLCs, highlighting the pivotal role of the land  
51 surface in modulating cloud formation and affecting the spatial and temporal  
52 distribution of low clouds (Zhang and Klein, 2010; 2013; Rieck et al., 2014; Xiao et al.,  
53 2018; Lareau et al., 2018; Lee et al., 2019; Tang et al., 2019; Tao et al., 2019; Tian et  
54 al., 2022).

55 These clouds, which frequently form in the PBL's entrainment zone, are very  
56 challenging to be simulated in weather prediction and climate modeling due to the small  
57 scales of their operating physics and the complex feedback mechanisms between land  
58 surface fluxes, PBL turbulent processes, and cloud microphysics (Miao et al., 2019; Lu  
59 et al., 2011; Fast et al., 2019; Morrison et al. 2020; Yang et al., 2018; Nogherotto et al.,  
60 2016; Caldwell et al., 2021; Wang et al., 2023; Guo et al., 2019). These challenges are  
61 compounded when attempting to represent such processes in global and regional  
62 climate models, where the fine-scale interactions are often parameterized in a coarse-  
63 resolution grid due to computational constraints (Bretherton et al., 2007; Zheng et al.  
64 2021; Moeng et al., 1996; Randall et al., 2003; Prein et al., 2015). In addition, different

65 cloud regimes exhibit complex nonlinear cloud-land interactions, which pose  
66 challenges for observational studies and modeling efforts, particularly for physical  
67 parameterizations (Tang et al., 2018; Qian et al., 2023; Sakaguchi et al., 2022; Poll et  
68 al., 2022; Tao et al., 2021).

69 As an emerging tool, machine learning (ML) has been widely employed for a  
70 variety of environmental and atmospheric studies (e.g., McGovern et al., 2017; Gagne  
71 et al., 2019; Vassallo et al., 2020; Cadeddu et al., 2009; Molero et al., 2022; Guo et al.,  
72 2024). Specifically, ML techniques are increasingly being employed to simulate and  
73 estimate convection and precipitation, which are crucial for accurate weather  
74 forecasting and climate modeling (Mooers et al., 2021; Wang et al., 2020; O'Gorman et  
75 al., 2018; Gentine et al., 2018; Zhang et al., 2021). For example, Rasp (2020) presents  
76 algorithms for the implementation of coupled learning in cloud-resolving models and  
77 the super parameterization framework. Similarly, ML tools have been applied to  
78 leverage observational data for the refinement of convection parameterizations, offering  
79 more insights into convective triggering (Zhang et al., 2021). In addition, ML has been  
80 used to emulate convection schemes and develop parameterizations using data from  
81 advanced simulations (O'Gorman and Dwyer, 2018; Gentine et al., 2018). Furthermore,  
82 Haynes et al. (2022) develop pixel-based ML-based methods of detecting low clouds,  
83 with a focus on improving detection in multilayer cloud situations and specific attention  
84 given to improving cloud characteristics. Despite the considerable advancements  
85 brought by ML, there are persistent challenges in accurately simulating the vertical  
86 structure of clouds, as well as their complex relationships with land surface.

87 Southern Great Plains (SGP) site, as part of the U.S. Department of Energy  
88 Atmospheric Radiation Measurement (ARM) program, is crucial for cloud evaluation  
89 and climatology studies in modeling efforts. Recognized globally as a leading climate  
90 research facility, the ARM SGP site (36.607°N, 97.488°W) has been collecting a wealth  
91 of meteorological and radiative measurements, offering data that spans over two  
92 decades (Sisterson et al., 2016). The rich dataset from the ARM SGP site can help  
93 address persistent challenges in cloud modeling. This study leverages these extensive  
94 observations to build a deep learning model, serving as an observation-based  
95 "emulator" for simulating BLCs. Our model enhances the estimations for cloud fields  
96 of BLCs, particularly cloud occurrence, position, and fraction. Furthermore, the critical  
97 assessment of our model in comparison with existing reanalysis datasets, including  
98 MERRA-2 and ERA5, highlights the improvement in estimating cloud vertical  
99 structure. Our study analyzed the model's performance across different cloud regimes,  
100 such as stratiform and cumulus. By undertaking this endeavor, we aim to help bridge  
101 the existing gaps between field observations and modeling by a deep learning model of  
102 BLCs, thereby improving diagnostics of model performance and enriching our  
103 understanding of the BLC processes.

104

## 105 **2 Data Description**

### 106 **2.1 Observations for the development of the deep learning model**

107 This study utilized the ARM SGP observations during 1998-2020 to serve as  
108 training, validation, and testing data for the development of the deep learning model.

109 Note that all the observations are collected at the central facility of SGP, a fixed location,  
110 which is different from other ML studies that use global data from reanalysis or climate  
111 model simulations (e.g., O’Gorman and Dwyer, 2018; Shamekh et al., 2023).

112 The input data to train and validate the deep learning model include early morning  
113 sounding data and diurnal varying surface meteorological conditions and surface  
114 turbulent heat fluxes. We take radiosondes (SONDE) measurements around 6 a.m.  
115 local time to offer thermodynamic and wind profiles in the PBL and the free atmosphere  
116 as initial conditions (Holdridge et al., 2011). SONDE launches typically took place four  
117 times per day at the SGP site, usually at 00, 06, 12, and 18 local times. Local time,  
118 defined as daylight saving time, is used consistently throughout the year. Each morning  
119 profile comprises 46 levels spanning from 0-8 km, which include levels at intervals of  
120 50 meters from 0 to 1 km, 0.1 km from 1 to 2 km, 0.25 km from 2 to 4 km, and 0.5 km  
121 from 4.5 to 8 km. Meanwhile, the collocated surface meteorology systems (MET,  
122 Ritsche, 2011) provide a variety of meteorological measurements (i.e., temperature,  
123 relative humidity, wind, and pressure) at the surface. Surface sensible and latent heat  
124 fluxes are taken from the ARM value-added product called the best-estimate fluxes  
125 from the Bulk Aerodynamic calculations of the Energy Balance Bowen ratio  
126 measurements (BAEBBR, Cook, 2018).

127 In addition, we also use derived variables based on observations as the input fields  
128 into the deep learning model. LCL is derived from the surface meteorology (Romps,  
129 2017),  $BLH_{\text{parcel}}$  (boundary layer height derived from parcel methods) is calculated  
130 from the morning temperature profiles and surface air temperature (Holzworth, 1964;

131 Su and Zhang, 2024; Chu et al., 2019). Specifically,  $BLH_{\text{parcel}}$  is defined as the height  
132 where the morning potential temperature profile first exceeds the current surface  
133 potential temperature by more than 1.5 K. Meanwhile,  $BLH_{\text{SH}}$  (boundary layer height  
134 derived from sensible heat flux) is calculated from the morning temperature profiles  
135 and surface sensible heat (Stull, 1988; Su et al., 2023).

136 For the target data of model outputs to train and validate the deep learning model,  
137 our study employs hourly cloud fraction data available from the ARM Best Estimate  
138 (ARMBE, Xie et al, 2010) dataset. This cloud fraction is developed based on the Active  
139 Remote Sensing of Clouds (ARSCL, Clothiaux et al., 2000, 2001; Kollias et al., 2020),  
140 which utilizes the best estimates from ceilometer for the lowest cloud bases and  
141 integrates micro-pulse lidar, ceilometer, and cloud radar data to define cloud tops and  
142 cloud fraction. In addition, to construct learning targets, the base of BLC is determined  
143 at the lowest altitude where the cloud fraction first exceeds 1 %, and the cloud top is  
144 identified at the point where the cloud fraction transitions from exceeding 1 % to falling  
145 below this threshold. In multi-layer systems, the DNN model is trained based on the  
146 lowest cloud layer when it is coupled with the land surface. However, we do not exclude  
147 multiple-layer cloudy cases if their vertical fractions are continuous from the lower to  
148 upper layer.

149 Based on ARM observations, this study develops an advanced deep-learning  
150 framework to simulate the BLCs, using detailed observational data, including SONDE  
151 profiles, surface meteorological measurements, and ARSCL, from the SGP site. This  
152 framework is designed for BLCs, placing a particular emphasis on cloud-land coupling

153 mechanisms. By integrating morning SONDE observations with diurnally varying  
154 surface fluxes and meteorological data, this deep learning model is capable of  
155 diagnosing the initiation and evolution of low clouds, especially those coupled with  
156 land surface processes.

157

## 158 **2.2 Classification of coupled boundary layer clouds from observations**

159 The deep learning model in this study aims to simulate BLCs strongly coupled with  
160 boundary layer and land surface processes. The classification of clouds below is to filter  
161 the BLCs based on the concept of cloud-land coupling and is important for the training  
162 and analysis of the deep learning model. Here, we treat BLCs as synonymous with land-  
163 coupled clouds, in contrast to clouds that are decoupled from the PBL and land surface.

164 Coupled clouds are identified when the cloud base height (CBH), as derived from  
165 the ceilometer, aligns with or is below the lidar-detected PBL top height within 0.2 km,  
166 and the calculated surface-based Lifting Condensation Level (LCL, Romps, 2017) falls  
167 within a maximum allowable range of 0.7 km (Su et al., 2022). PBL height data (Su et  
168 al., 2020; Roldán-Henao et al., 2024) are available through the ARM database. This  
169 alignment is indicative of clouds that are directly influenced by surface-driven  
170 processes. Meanwhile, a cloud thickness threshold ( $< 4$  km) is applied to ensure the  
171 occurrence of BLCs (i.e., not deep convective clouds).

172 Within the scope of land-coupled clouds, we further classify the observed daytime  
173 BLCs into cumulus and stratiform categories following the methodology in Su et al.  
174 (2024). Stratiform cloud days are identified by prolonged overcasting conditions during



175 the daytime, lasting more than three hours, with the maximum cloud fraction exceeding  
176 90 % based on ARSCL data. For cumulus cloud days, two criteria are applied: (1) cloud  
177 formations emerge after sunrise, ensuring that they are driven by local convective  
178 processes, and (2) there is an absence of stratiform clouds. Based on these criteria, we  
179 identified 940 days categorized under the cumulus regime, distributed as 21 %, 56 %, 17 %, and 6 %  
180 across Spring, Summer, Fall, and Winter, respectively. Similarly, we  
181 identified 657 days falling within the stratiform clouds regime, with respective seasonal  
182 distributions of 37 %, 12 %, 23 %, and 28 %. Note that this cloud regime classification  
183 is done on a daily basis. To maintain clarity in our analysis, we excluded days with  
184 mixed cloud regimes, focusing only on days that exhibit only stratiform or cumulus  
185 clouds during the daytime.

186

### 187 **2.3 Reanalysis data for the application of the deep learning model**

188 To demonstrate how to use the deep learning model, we take advantage of  
189 reanalysis datasets from the European Centre for Medium-Range Weather Forecasts'  
190 fifth-generation global reanalysis (ERA5, Hersbach et al., 2020) and NASA's Modern-  
191 Era Retrospective analysis for Research and Applications Version 2 (MERRA-2, Gelaro  
192 et al., 2017). Note that unlike observational data aforementioned, reanalysis data are  
193 not used for training the deep learning model, instead they are going to be used to help  
194 illustrate how the deep learning model may disentangle the potential causes leading to  
195 the biased cloud simulations.

196 ERA5 provides hourly atmospheric states and cloud fraction around SGP by the

197 Integrated Forecasting System (IFS) and a data assimilation system at a horizontal  
198 resolution of  $0.25^\circ \times 0.25^\circ$  and a vertical resolution of 25 hPa in the lower atmosphere  
199 (700 – 1000 hPa). IFS employs a prognostic cloud scheme capable of capturing the  
200 evolution of cloud dynamics over consecutive time steps (Tiedtke, 1993), a feature that  
201 enhances its utility in time-dependent climate studies.

202 MERRA-2 provides hourly low cloud fraction and 3-hourly vertical cloud  
203 fraction profiles at a spatial resolution of  $2/3^\circ$  (longitude)  $\times$   $1/2^\circ$  (latitude). MERRA-  
204 2 is based on the Goddard Earth Observing System Data Assimilation System Version  
205 5 and utilizes a diagnostic cloud scheme, focusing on the immediate state of clouds  
206 (Randles et al., 2017), which are widely used in multiple studies (e.g., Yeo et al., 2022;  
207 Kuma, 2020; Miao et al., 2019).

208 Here we acknowledge the local heterogeneity of cloud fields in the area covered  
209 by an ERA5 or MERRA-2 grid cell. This inherent discrepancy between the reanalysis  
210 data and the ARM SGP observations may arise from the difference between point-based  
211 measurements and area-based assimilated grid-averages. However, observations at the  
212 SGP site, representative of plain regions, have been widely used for evaluating models  
213 across scales from climatological and statical perspectives (e.g., Song et al., 2014; Zhao  
214 et al., 2017; Zheng et al., 2023; Zhang et al., 2017).

215

## 216 **3 Construction of the Deep Learning Model for Boundary Layer Clouds**

### 217 **3.1 Structure design of the deep learning model**

218 This study develops an integrated deep learning model to simulate BLC over the  
219 SGP site, whose design is illustrated in Fig. 1. Traditionally, simulating BLCs involves  
220 solving complex equations related to PBL turbulence and cloud microphysical  
221 processes. Our approach, however, leverages deep learning to bypass these intricate  
222 simulations. By using module-specific hidden layers, the deep learning model serves as  
223 an observation-based "emulator" that directly estimates BLCs from early-morning  
224 soundings and surface-related parameters.

225 The model is purpose-built to consist of three distinct deep learning modules, each  
226 responsible for a critical aspect of the cloud simulation: 1) the determination of the  
227 BLC occurrence, 2) the height position of the cloud base, and 3) the cloud thickness  
228 and the normalized 10-layered shape of cloud fraction within cloud boundaries, which  
229 jointly yield the hourly-averaged vertical structures of BLCs. This modular approach  
230 ensures that the estimations are specific for each aspect of the BLCs. Combining cloud  
231 thickness and cloud fraction in one module is logical because the thickness for 10-  
232 layered clouds varies based on cloud thickness, and thickness is potentially related to  
233 the fraction, as thicker clouds are sometimes associated with larger cloud fractions.  
234 Naturally, cloud top is considered as the cloud base plus the thickness. This separation  
235 of tasks enhances the overall reliability and clarity of the model in capturing the various  
236 characteristics of BLCs. Note that each of the three deep learning modules is built  
237 upon a deep neural network (DNN) with multiple hidden layers.

238 The occurrence module, as the first step, evaluates the likelihood of cloud  
239 formation by producing a number between 0 and 1, which we call “trigger” in the  
240 following, whose value above 0.5 indicates the presence of clouds. The target data for  
241 this module is binary (0 or 1), and the model output is a continuous value between 0  
242 and 1. This occurrence information then feeds into the other two modules in parallel:  
243 one for locating cloud boundaries and the other for delineating the vertical shape of the  
244 cloud fraction in cloudy layers. While the cloud-base (or boundary) module and the  
245 fraction-thickness (or fraction) module are independent of each other, they collaborate  
246 to depict the vertical cloud fraction profile.

247 To represent the vertical structure of BLC in the fraction-thickness module, we  
248 segmented the cloud layer from the base to the top into ten levels, with each level's  
249 thickness varying according to the overall cloud thickness. These values are then  
250 interpolated to create a continuous vertical profile of cloud fraction within the BLC  
251 boundaries, offering a detailed depiction of the cloud's vertical extent. The vertical  
252 position of the layer changes based on the predicted cloud base and top to accurately  
253 represent the vertical structure of BLCs. This dynamic approach allows the fraction  
254 module to adjust and focus on the relevant portions of cloud fraction within cloudy  
255 layers. Compared to a static height-level approach, which requires the prediction of  
256 cloud fraction across a fixed vertical extent (e.g., multiple levels between 0-6 km), our  
257 method focuses on the shape of the fraction profile. This ensures the model is not  
258 constrained by fixed vertical levels, allowing for more efficient and robust estimations.

259

## 260 3.2 Deep Neural Network (DNN) architecture and configuration

261 The construction of the deep learning model uses the TensorFlow Package,  
262 developed by Google (<https://www.tensorflow.org/>). Each module in the deep learning  
263 model is constructed based on a separate deep neural network (DNN) respectively. The  
264 DNN architecture is designed, beginning with an input layer reflective of the selected  
265 feature set, which includes morning sounding profiles, surface meteorology and heat  
266 fluxes data, and the derived variables such as LCL, BLH<sub>parcel</sub> and BLH<sub>SH</sub>. For predicting  
267 the current hour BLC, the inputs of surface conditions include data both at the current  
268 hour and the previous hour. The input variables for training and validating the deep  
269 learning model are detailed in Table 1, including variable names, descriptions, and data  
270 sources, together with the ARMBE cloud fraction profiles as the learning target for  
271 model outputs. Normalization, a preprocessing technique, was applied to both input and  
272 target data to scale them to a zero mean and a standard deviation of one (Klambauer et  
273 al. 2017; Salimans and Kingma, 2016; Raju et al. 2020). This standardization ensures  
274 that the data is scaled to a common range and offers some benefits, such as improving  
275 the stability and efficiency of the training process.

276 The architecture of the DNN models was structured and tailored for each module:  
277 occurrence, cloud-base, and fraction (or fraction-thickness) estimation. Each module's  
278 structure is defined by the number of neurons in its hidden layers. For the occurrence  
279 module, the structure consists of four hidden layers with 108, 64, 36, and 24 neurons,  
280 respectively. The CBH prediction module is similarly structured with four hidden layers,  
281 but consisting of 96, 56, 32, and 24 neurons, respectively. The module for predicting

282 cloud fraction and thickness has a slightly simpler structure, with three hidden layers  
283 containing 56, 32, and 24 neurons, respectively.

284 As the specific configuration, we utilized the ReLU (Rectified Linear Unit)  
285 activation function to introduce non-linearity into the DNN. L2 regularization with a  
286 strength of 0.01 is applied to mitigate overfitting by penalizing large weights and  
287 encouraging simpler models. Batch normalization is implemented at each layer to  
288 normalize the inputs, ensuring consistent data distribution and stabilizing the learning  
289 process. A dropout rate of 0.2 is used to randomly omit neuron connections during  
290 training, preventing overfitting and encouraging the network to learn more robust  
291 features. The training process was refined with early stopping, ceasing further epochs  
292 when the validation loss ceased to improve, and learning rate reduction, systematically  
293 decreasing the learning rate upon encountering plateaus in performance improvement.  
294 These callbacks were instrumental in honing the model's performance, ensuring  
295 convergence to the accurate estimation of the BLC. Neuron biases are included in the  
296 network's architecture and systematically inserted in the hidden layers (Battaglia et al.  
297 2018). The model is compiled using the Adam optimizer with an initial learning rate of  
298 0.01. The loss functions used are mean squared error for regression tasks and Binary  
299 Cross-Entropy for binary classification tasks. The batch size during training is set to 32.  
300 Early stopping with a patience of 37 epochs is implemented to prevent overfitting and  
301 to restore the best weights when the validation loss ceases to improve.

302

### 303 **3.3 Model Training Process and Examples**

304 The construction of the deep learning model commences with the segregation of the  
305 ARM observations into a training subset (70 %) and a validation subset (30 %) during  
306 1998-2016. In addition, we save data from 2017-2020 for testing, specifically focusing  
307 on this independent period to assess the model's performance. Upon training completion,  
308 the model is then evaluated, with its performance metrics examined for accuracy and  
309 reliability. This methodical and data-driven process balances complexity with precision,  
310 culminating in a robust model capable of simulating BLC features.

311 The modules within the deep learning model operate synergistically, with the  
312 predicted occurrence of clouds extending into the modules for cloud base and the  
313 vertical structure (i.e., cloud thickness and shape of the cloud fraction profile). As the  
314 example of the model output, Fig. 2 offers a comparative display of diurnal cloud  
315 fraction profiles over the SGP, contrasting the observed data with the simulated clouds  
316 by the deep learning model. The model accurately simulates the cloud occurrence and  
317 the CBH for these cases, aligning well with observations. However, it falls short in  
318 simulating the cloud top heights, especially significant overestimates for stratiform  
319 clouds. It also underestimates maximum cloud fractions for the stratiform clouds. The  
320 observed maximum cloud fraction for stratiform is close to 1, indicating complete  
321 coverage, however, such an aspect is not fully replicated by the deep learning model.  
322 The third case also falls into the category of stratiform clouds, characterized by an  
323 observed cloud fraction exceeding 0.9. However, the presence of multiple local maxima  
324 within the cloud fraction profile indicates a relatively complex structure. This

325 complexity poses a challenge to the model, as the DNN is not fully capable of capturing  
326 the internal variations within the convective system. Instead, the model tends to produce  
327 a more uniform cloud fraction across this convective system. Despite these variances,  
328 the model-derived cloud bases and occurrence demonstrate high consistency with  
329 observations, highlighting its value in the cloud simulations.

330

### 331 **3.4 Calculations of Feature Importance and Performance Metric**

332 To elucidate the significance of each input variable within our deep learning models,  
333 we implemented a permutation importance analysis. This robust, model-agnostic  
334 technique assesses each feature's influence on the model's predictive accuracy, which  
335 is crucial for assessing DNN (Date and Kikuchi, 2018; Altmann et al. 2010). In this  
336 study, the permutation importance method differs slightly for each module within the  
337 deep learning model based on whether the module's task is regression (cloud-base and  
338 fraction-thickness) or classification (occurrence).

339 For the modules of cloud-base and fraction-thickness, which are regression tasks,  
340 the Mean Absolute Error (MAE) serves as the performance metric. First, we perform a  
341 test run to establish a baseline performance by calculating the MAE of the module using  
342 the original, unperturbed validation datasets, which comprise early-morning sounding,  
343 surface conditions and the derived variables as the inputs. Then, for every input feature  
344 in the validation set, we disrupt its association with the target cloud fields by shuffling  
345 its values across all instances, creating a permutation of the dataset. This is executed



346 while maintaining the original order of other features. When performing the  
347 permutation, we shuffle the entire morning profile for each case without altering the  
348 internal height order of values within the profile. This approach ensures that while  
349 profiles are permuted across different cases, the sequential structure of height values  
350 within each profile remains intact. This method allows us to assess the importance of  
351 the profiles as coherent units, rather than disrupting their vertical structures.  
352 Furthermore, we re-run the DNN modules with the shuffled feature and all other  
353 features intact as inputs and recalculate the MAE with the new outputs. The difference  
354 between this new MAE and the baseline MAE represents the feature's importance. To  
355 ensure a comprehensive assessment, the permutation and the subsequent MAE  
356 calculation are repeated 20 times with different random shuffles for each input feature.  
357 The final importance score for each feature is then determined as the mean increase in  
358 MAE across these permutations.

359 For the module of cloud occurrence, which is a classification task, the accuracy  
360 score is used as the performance metric. The accuracy score is a measure of the model's  
361 overall correctness and is calculated using the formula:

$$362 \quad Accuracy = \frac{TP + TN}{TP + TN + FP + FN} \quad (1)$$

363 where True Positives (TP) indicates the number of instances correctly predicted as  
364 positive; True Negatives (TN) indicates the number of instances correctly predicted as  
365 negative; False Positives (FP) indicates the number of instances incorrectly predicted  
366 as positive, and False Negatives (FN) indicates the number of instances incorrectly  
367 predicted as negative. After determining the performance metric, other procedures for

368 determining feature importance remain the same between regression tasks and the  
369 classification task.

370 After determining the importance scores from the test run, in refining the model,  
371 features contributing a negligible or negative effect on performance (i.e., importance  
372 scores less than zero) are excluded to ensure only beneficial data is used.

373 By using this methodology, Fig. 3 illustrates these importance scores from different  
374 features, underscoring the most influential factors for predicting the BLC occurrence,  
375 the cloud-base, and the thickness and the shape of the vertical fraction of BLCs. These  
376 factors are ranked from most important factors to least important factors. Notably, the  
377 importance scores are not computed as a simple sum but are determined by collectively  
378 shuffling groups of features and observing the impact on model performance. The BLC  
379 trigger of occurrence is a special factor since it is the output of the classification model.  
380 The trigger value, which indicates the likelihood of cloud occurrence, is used as an input  
381 to the estimations of cloud boundaries and fractions. Sometimes, the trigger value  
382 hovers around 0.5, indicating uncertainty about the presence of clouds. This situation  
383 often corresponds to scenarios like broken clouds or residual clouds, typically  
384 associated with relatively small cloud fractions. Incorporating the trigger value as an  
385 input for cloud fraction estimation helps the model account for these ambiguous  
386 situations, thereby enhancing its ability to estimate cloud fraction. Specifically, only  
387 trigger values greater than 0.5 indicate cloud presence and are used for cloud fraction  
388 predictions. While including the trigger value is beneficial for the cloud fraction model,  
389 it does not affect the CBH estimation.

390 In particular, surface relative humidity (RH), surface air temperature (T), and  
391 morning relative humidity profiles are highly influential in BLC simulations. This is  
392 consistent with previous observational and modeling studies (Zhang and Klein, 2013).  
393 Surface RH is a critical factor affecting the occurrence, CBH, and cloud fraction  
394 predictions. As the input conditions for the DNN modules, early-morning atmospheric  
395 profiles of different meteorological parameters (i.e., RH, temperature, and wind  
396 components) exert a notable impact on cloud occurrence detection and the  
397 determination of cloud fractions. Surface air temperature is shown to have a substantial  
398 effect on cloud fraction, highlighting the sensitivity of cloud simulations to near-surface  
399 thermal conditions. Meanwhile,  $BLH_{\text{parcel}}$  demonstrates a notable impact, which is  
400 understandable since the PBLH is a critical factor for the formation of BLCs, and  
401  $BLH_{\text{parcel}}$  provides a good representation of PBLH. This approach also recognizes the  
402 interconnectedness of certain features and their collective contribution to the model's  
403 output.

404

## 405 **4 Boundary Layer Cloud Simulations by the Deep Learning Model**

### 406 **4.1 The Occurrence of Boundary Layer Clouds**

407 The occurrence of BLC is a multifaceted process influenced by a variety of  
408 atmospheric parameters and surface processes. As a critical component in the formation  
409 of BLCs, we utilize the deep learning model to identify the BLC trigger using morning  
410 meteorological profiles and observed surface meteorology and fluxes. Figure 4  
411 showcases the model's proficiency in classifying the occurrences (class 1) and non-

412 occurrences (class 0) of BLC during both a trained period and an independent period.  
413 The classification significantly affects the statistical estimation of cloud fraction, as  
414 cloud fraction is set to 0 if the trigger is less than 0.5. The confusion matrices (Luque  
415 et al. 2019) for the trained period (1998-2016) and for the independent period (2017-  
416 2020) display the model's predictive performance. The matrices reveal the counts and  
417 percentages of TP, FP, TN, and FN. For the training period, we use a 70 % training and  
418 30 % validation split to ensure model validation and use the validation dataset to  
419 generate the statistics. Meanwhile, for the independence period, we use the full dataset  
420 for the validation.

421 Figure 4a represents the trained period, the validation datasets show a high  
422 percentage of TN at 71.2 % and TP at 21.1 %, indicating that the model is accurate  
423 during the period it was trained. For the independent period (2017-2020), the model  
424 still performs well, with 71.8 % TN and 17.4 % TP (Fig. 4b). However, the rates of FN  
425 and FP are slightly higher at 5.6 % and 5.2 % respectively, which could indicate that  
426 the model is slightly less accurate when applied to data beyond its training scope. The  
427 table highlights the model's robustness, with overall accuracy rates of 92.3 % for the  
428 trained period and a slightly reduced but still substantial 89.2 % for the independent  
429 period. Moreover, for the trained period, the model achieved a high precision of 88.1 %  
430 and a recall of 81.2 %. For the independent period, the precision and recall remained  
431 reasonably high at 76.9 % and 75.6 %, respectively, demonstrating the model's effective  
432 generalization to new data. These metrics demonstrate the model's predictive  
433 capabilities and reliability for both trained and independent periods.

434 Figure 5 further compares the diurnal frequency of BLC occurrence between  
435 observations (OBS) and the DNN predictions for different seasons. The BLC's strong  
436 diurnal pattern is well-captured by the model, when BLC development peaks between  
437 12-16 local times, aligning closely with observed frequencies. Among different seasons,  
438 the model is notably effective in simulating the pronounced diurnal cycle of summer  
439 clouds, which are typically influenced by local convection. Conversely, the winter  
440 season exhibits a weaker diurnal pattern, likely linked to the diminished surface fluxes.  
441 The DNN tends to overestimate BLC presence in the early morning, especially for the  
442 winter season. The overall alignment between observations and the DNN module  
443 represents the model's capability of capturing the diurnal patterns of BLC formation  
444 and development. Determining the occurrence of BLC lays the foundation for the  
445 integrated simulations of BLC features.

446

## 447 **4.2 Cloud Boundaries and Fraction**

448 A key aspect of cloud modeling involves the accurate simulation of cloud  
449 boundaries and fraction, which are indicative of a cloud's vertical extent and fractional  
450 coverage at different height levels. Our deep learning model demonstrates capabilities  
451 in predicting these key attributes of BLC.

452 Figure 6 offer the comparisons between observed values and predictions by the  
453 DNN for CBH, CTH, and cloud fraction. Similarly, as in Sect. 4.1, these comparisons  
454 are presented for both the training period (a, c, e, based on validation datasets) and an

455 independent period (b, d, f), revealing the model's ability to generalize beyond its initial  
456 training data. The DNN model demonstrates remarkable performance in simulating  
457 cloud base, boasting a correlation coefficient surpassing 0.9 and an MAE under 0.15  
458 km. Conversely, the model encounters challenges with CTH prediction, evidenced by  
459 a lower correlation of about 0.5 and a significantly higher MAE between 0.8 and 0.9  
460 km, aligning with case studies in Fig. 2.

461 The discrepancy in accurately simulating CBH and CTH may stem from two main  
462 factors. Firstly, observed CBH determinations are generally more precise due to the  
463 effectiveness of laser-based methods (Pal et al., 1992), while observed CTH estimations  
464 often suffer from reduced accuracy, partly attributed to signal attenuation issues  
465 (Clothiaux et al., 2000). For the observed shallow cumulus, cloud top is often  
466 contaminated by insect signals, further complicating accurate CTH measurements  
467 (Chandra et al., 2010). Secondly, our DNN simulations are developed from the  
468 perspective of cloud-land coupling, primarily utilizing surface meteorology. This can  
469 introduce inherent limitations, as the tops of many clouds may be decoupled from  
470 surface influences despite a coupled base, potentially leading to gaps in the DNN's  
471 ability to accurately define and estimate the cloud top.

472 The comparison of cloud fraction between observations and DNN is presented to  
473 consider the model's capability to simulate the vertical distribution of cloud coverage  
474 (Fig. 6e-f). The scatterplots comparing observed and modeled cloud fractions at  
475 individual levels in cloudy scenarios show a satisfactory correlation, with an R-value

476 exceeding 0.77 and an MAE around 0.15. Nevertheless, the DNN model tends to  
477 underestimate the peak cloud fraction, displaying a range up to ~0.8 compared to the  
478 full 0-1 range observed. This underestimation is intrinsically linked to the model's  
479 simulation of cloud boundaries, as both cloud fraction and cloud-base modules operate  
480 in tandem. For stratiform clouds, observational data typically exhibit a relatively  
481 uniform vertical extent with cloud fractions close to unity at the central height, whereas  
482 the DNN model tends to generate a broader, more attenuated profile with a reduced  
483 maximum cloud fraction at the center. This points to a need for refining the model's  
484 ability to replicate the pronounced peak cloud fractions characteristic of stratiform  
485 cloud profiles.

486       The diurnal patterns of cloud base and top heights, captured through daily profiles,  
487 showcase the model's adeptness at simulating the temporal changes in cloud positions  
488 for all BLCs, the cumulus regime, and the stratiform regime (as shown in Fig. 7). These  
489 profiles, derived from both observational data and DNN outputs, include shaded regions  
490 representing the variability (one standard deviation) around the average heights.  
491 Cumulus clouds exhibit a marked diurnal cycle, whereas stratiform clouds typically  
492 maintain a relatively constant cloud boundaries and smaller variations throughout the  
493 day. A close alignment is observed between the mean and standard deviation of the  
494 cloud base between the observed and the simulated data for different cloud regimes. In  
495 contrast, while the mean cloud top heights follow a similar diurnal trend in both cases,  
496 the observed data exhibits more pronounced variabilities compared to the relatively  
497 small variabilities in the DNN simulations.

498        Figures 6 and 7 collectively demonstrate the model’s ability to simulate cloud  
499 boundaries and fractions within BLC. It reliably captures CBH yet encounters  
500 challenges with accurately representing cloud top heights and peak cloud fractions on  
501 an individual basis. These constraints are somewhat expected, given that even very fine-  
502 scale models struggle to entirely capture the vertical extent of clouds, as evidenced in  
503 Large-Eddy Simulations or Convection-Permitting Models (Zhang et al. 2017;  
504 Gustafson et al. 2020; Bogenschutz et al. 2023). In addition to the discussion of deep  
505 learning models, we also acknowledge the role of mixed-layer (single-column) models  
506 in representing boundary layer processes (Lilly 1968, Pelly and Belcher, 2001; Clayson  
507 and Chen, 2002; Zhang et al, 2005, 2009; De Roode et al., 2014). Mixed-layer models  
508 have several advantages: they are inherently grounded in physical principles and are  
509 readily integrated into many large-scale models. These models are effective at capturing  
510 the diurnal evolution of the PBL given an initial state and time series of surface fluxes.  
511 However, the DNN approach offers distinct benefits that complement this theoretical  
512 approach. DNNs might be able to capture complex, nonlinear relationships between  
513 various controlling factors and the cloud fraction. These may be difficult to capture by  
514 the single (for the overcast stratocumulus-topped mixed layer) or multiple mixed-layer  
515 models (for the broken trade cumulus clouds), which are still subject to assumptions,  
516 e.g., on entrainment processes. By training on large observational datasets, DNNs can  
517 learn from real-world examples, potentially identifying patterns and relationships not  
518 explicitly encoded in physical models.

519



## 520 **5 Application of the Deep Learning Model**

### 521 **5.1 Integration with Reanalysis Datasets**

522 As shown in Sect. 4, the deep learning model can take the conventional  
523 meteorological observations (i.e. morning SONDE and surface conditions) as inputs to  
524 simulate the BLC as outputs, reasonably reproduce a good agreement with the observed  
525 vertical structures of BLCs. For its potential application, we may treat it as an “emulator”  
526 of the observed relationships between input and output variables. Here we present an  
527 example by integrating the deep learning model with ERA5 and MERRA-2 to simulate  
528 BLC with the input of early-morning profiles and surface conditions from the reanalysis.  
529 Here we ask, if inputs are treated as “reality”, what would be the expected responding  
530 cloud fraction simulated by the deep learning model, an observation-based emulator?

531 Following these thoughts, Fig. 8 contrasts diurnal cloud fraction patterns from the  
532 observational data and the deep learning model predictions averaged over all conditions  
533 of seasons and years. Figure 8a-b present the observed cloud fractions and those  
534 simulated by the deep learning using ARM data as inputs, respectively. Panels c and e  
535 show the cloud fractions directly extracted from ERA5 and MERRA-2 reanalysis  
536 datasets, while panels d and f illustrate the simulated cloud fraction by the deep learning  
537 model using inputs from ERA (ERA<sub>DNN</sub>) and MERRA (MERRA<sub>DNN</sub>) reanalysis data.  
538 Observing fluctuations in surface temperature and humidity data in ERA5 for this  
539 region, we smoothed ERA5 surface air temperature and humidity data with a  $\pm 1$ -hour  
540 window to mitigate potential variability from assimilation before using them as input  
541 for the DNN modules. To eliminate sampling biases in comparison, we averaged only

542 those samples for which both observations and reanalysis are concurrently available.

543 Note that here we adopt the deep learning model as a complementary tool rather  
544 than a replacement for any existing cloud representations in reanalysis data. The DNN  
545 outputs serve a diagnostic purpose, identifying biases in BLCs and aiding in  
546 understanding deficiencies within reanalysis data.

547 The DNN simulations with ARM observations as inputs align closely with the ARM  
548 observed cloud fraction profiles within the 0-2 km range, reflecting the model's ability  
549 to capture land-coupled clouds. As this model is designed for diagnosing land-coupled  
550 clouds, the model does not simulate decoupled clouds, which often have bases  
551 occurring above 2-km (Su et al., 2022). Original cloud data directly from reanalysis  
552 show significant underestimations of BLC fractions, particularly evident in MERRA-2.  
553 The application of the deep learning model using reanalysis data as inputs enhances  
554 cloud fraction estimations compared to the original cloud data directly from reanalysis,  
555 demonstrating the DNN model's strength in simulating BLC. Given that the DNN  
556 model specializes in simulating BLC, when utilizing reanalysis data, the portion of  
557 cloud profiles that are decoupled are preserved as they are in the original datasets—that  
558 is, for the cloud layers above the BLC-tops or as those clouds rooted above the PBL.

559 Furthermore, Fig. 9 provides a detailed examination of stratiform clouds, utilizing  
560 the same comparative approach as in Fig. 8. The observed stratiform clouds display a  
561 layered structure with expansive coverage and maximum cloud fractions typically  
562 exceeding 0.6. The DNN model using ARM data as inputs reproduces these observed  
563 characteristics fairly well, albeit with minor overestimations in cloud vertical extent.

564 Conversely, the original ERA5 and MERRA-2 stratiform cloud data exhibit limitations,  
565 particularly in underestimating cloud fraction. The integration of the DNN model with  
566 reanalysis data as inputs enhances the estimations of stratiform cloud fractions, as  
567 depicted in the heatmaps of Fig. 9, showcasing improved agreement with observational  
568 data and underscoring the enhancement potential for cloud fraction simulations in  
569 reanalysis datasets.

570 In addition, Fig. 10 extends the comparative study to cumulus clouds. Cumulus  
571 clouds pose significant challenges for modeling and parameterization partly due to their  
572 typically small spatial extent compared to the model grid, often spanning from a few  
573 hundred meters to several kilometers (Zhang et al. 2017; Tao et al., 2021; Bogenschutz  
574 et al. 2023; Gustafson et al. 2020). In line with expectations, the original ERA5 and  
575 MERRA-2 cloud fields exhibit significant biases in representing cumulus clouds when  
576 compared to observational data. In contrast, the DNN model with ARM data as inputs  
577 achieves commendable success in capturing the diurnal variability of cumulus clouds,  
578 including cloud base, vertical extension, and cloud fraction, by leveraging local  
579 convective signals derived from surface meteorology data. When the DNN model is  
580 integrated with ERA5 as inputs, it significantly improves the estimation of vertical  
581 cloud fields of cumulus. However, the original MERRA-2 data, which tend to overlook  
582 the majority of cumulus clouds, continue to significantly underrepresent them even  
583 after the application of DNN, suggesting that additional biases in the input variables  
584 such as meteorological factors may contribute to this discrepancy.

585 The integration of deep learning with ERA5 and MERRA-2 reanalysis datasets

586 demonstrates the notable refinement in the simulation of BLC, and achieves more  
587 accurate estimations of cloud fractions for both stratiform and cumulus clouds.

588

## 589 **5.2 Applying Deep Learning for Bias Attribution in Cloud Simulation**

590 We further examine the remaining disparities in cloud fraction simulations within  
591 reanalysis datasets, despite the integration of deep learning models (as shown in Figs.  
592 8-10), indicating persisting meteorological biases. Deep learning is utilized to quantify  
593 and attribute these biases for BLC simulations.

594 Figure 11 offers a comparative analysis of vertical cloud fraction profiles for both  
595 stratiform and cumulus clouds. It presents cloud fractions directly taken from reanalysis  
596 data (RD), including ERA5 and MERRA-2, and their corresponding deep learning-  
597 informed simulations. While the application of deep learning to use reanalysis data as  
598 inputs ( $RD_{DNN}$ ) yields improvements, remaining cloud biases are evident, particularly  
599 in MERRA-2. Acknowledging the significant influence of surface RH on BLC  
600 simulations (as indicated by Fig. 3e, we refine the inputs into the DNN model by  
601 replacing the reanalysis surface RH with the ARM observed surface RH (the model  
602 output is labeled as  $RD_{DNN-RH}$ ). This modification leads to a much better simulation for  
603 MERRA-2, closing the gap with observational data, especially for stratiform clouds.  
604 For ERA5,  $RD_{DNN-RH}$  and  $RD_{DNN}$  show negligible differences for cumulus clouds, but  
605 for stratiform clouds,  $RD_{DNN-RH}$  also exhibits a reduced bias. These refined profiles of  
606 cloud fraction attest to the benefits of using the observed surface moisture data as input,  
607 confirming its important role in achieving a more accurate representation of BLC.

608 With such methodology, we may further dissect the bias in cloud fraction  
609 simulations attributed to various meteorological factors and the parameterization  
610 schemes within ERA and MERRA reanalysis datasets:

$$611 \quad \textit{Bias due to parameterization} = |RD - OBS| - |RD_{DNN} - OBS| \quad (2)$$

$$612 \quad \textit{Bias due to surface RH} = |RD_{DNN} - OBS| - |RD_{DNN-RH} - OBS| \quad (3)$$

613 where RD and OBS are the cloud fraction taken directly from reanalysis data and  
614 observations, respectively. The definitions of  $RD_{DNN}$  and  $RD_{DNN-RH}$  are the same as the  
615 above. For getting a representative value, these biases are layer-averaged from 0-4 km  
616 over different local times, and then normalized by the observed mean cloud fraction,  
617 offering a climatological perspective on the discrepancies between observed and  
618 simulated data across seasons and years. For equation (2), we assume that the  
619 climatology of observations used as input to the DNN model ( $OBS_{DNN}$ ) matches the  
620 observed cloud fraction climatology (i.e.,  $OBS_{DNN} \approx OBS$ ), which has been  
621 demonstrated in Figs. 9-11. Therefore, we exclude the term representing the difference  
622 between the DNN-predicted observations and the actual observations. This assumption  
623 justifies our approach by ensuring the input observations align with the observed cloud  
624 fraction in equations.

625 We get the bias attributed to different meteorological factors and parameterization  
626 schemes in the ERA5 and MERRA-2 datasets, respectively (Fig. 12). Each bar  
627 indicates the normalized bias contributed by factors such as morning meteorological  
628 profiles, surface pressure, surface fluxes, various surface meteorology variables, and  
629 parameterization schemes. Notably, parameterization stands out as a significant

630 contributor to bias, accounting for 14.45 % and 19.05 % of the discrepancy in stratiform  
631 clouds between observations versus ERA5 and MERRA-2 respectively. For cumulus  
632 clouds, the parameterization biases are more pronounced, contributing 22.23 % and  
633 30.94 % for ERA5 and MERRA-2, respectively.

634 In addition to parameterization, RH, RH profiles, and sensible heat are identified as  
635 major factors contributing to the differences between observations and reanalysis data.  
636 For instance, aligning MERRA-2's RH with observed surface RH could potentially  
637 reduce bias by 23.13 % for stratiform and 10.26 % for cumulus clouds. Meanwhile,  
638 surface RH and morning RH profiles in ERA5 lead to 11.25 % and 3.96 % of biases for  
639 the stratiform clouds. The bias between ERA5 and observed cumulus clouds is largely  
640 driven by parameterization, which suggests that employing the DNN model with ERA5  
641 can lead to a more accurate simulation of cumulus clouds.

642 The detailed bias attribution analysis facilitated by the deep learning model  
643 elucidates the individual impact of meteorological factors on the discrepancies in cloud  
644 fraction between observations and reanalysis data. It underscores the necessity for more  
645 accurate humidity data within reanalysis datasets to refine BLC simulations.  
646 Furthermore, this deep learning approach illuminates pathways for improved  
647 parameterization of boundary layer convection.

648

## 649 **6. Summary**

650 This study has developed a deep learning model to estimate the evolution of BLCs  
651 over the SGP. The model utilizes over two decades of meteorological data to simulate

652 BLC formation and characteristics, including the occurrence of BLCs, cloud boundaries,  
653 and vertical structures of cloud fraction. As this model is built based on the perspective  
654 of cloud-land coupling, the DNN approach demonstrates the capability to diagnose  
655 land-coupled convective systems from early-morning sounding and surface conditions.  
656 The DNN model is built on the cloud-land interactions and serves as the testimony for  
657 the coupling between BLCs and the land surface. The proficiency and reliability of the  
658 DNN model are evident in its robustness during both the training period and the  
659 subsequent independent periods. The deep learning model addresses the simulation of  
660 cloud vertical structure, among one of the key challenges in physics-based large-scale  
661 models. It should be noted that the current DNN model cannot produce detailed cloud  
662 microphysics and turbulence information. We propose using the DNN model alongside  
663 traditional physical models to obtain comprehensive information on BLCs.

664 The application of this model on the reanalysis datasets like ERA5 and MERRA-2  
665 has resulted in enhanced cloud field estimations for stratiform clouds and cumulus, and  
666 an accurate vertical structure of clouds in terms of climatology, providing a promising  
667 diagnostic tool for improving weather forecasting and climate modeling. The deep  
668 learning model notably addresses the limitation in cumulus simulations in the reanalysis  
669 data, Meanwhile, this approach is much more cost-effective compared to traditional  
670 parameterizations and schemes at various scales, as it can simulate two decades of  
671 BLCs with vertical information over the SGP within 1-minute using a single GPU node.

672 In addition to the BLC simulations, the deep learning model developed in this study  
673 also is used to attribute discrepancies between observational data and reanalysis

674 datasets to different meteorological factors. Besides parameterization, surface RH,  
675 morning RH profiles, and surface sensible heat are the three major factors that lead to  
676 the mismatches in BLC representation in ERA5 and MERRA-2. These findings  
677 underscore the importance of incorporating more accurate humidity information in  
678 reanalysis datasets, which is crucial for refining BLC simulations. This analysis also  
679 sheds light on the necessity to update reanalysis datasets with improved  
680 parameterization of boundary layer convection.

681       Moving forward, future work is warranted to test and extend this diagnostic tool to  
682 different synoptic patterns over a large region, which can be integrated into multiple-  
683 scale models or reanalysis data. However, several challenges need to be addressed to  
684 achieve this. One significant limitation is the lack of high-quality, detailed observations  
685 of clouds and radiosonde profiles globally. This scarcity of data can hinder the model's  
686 ability to generalize effectively across different regions. To overcome this, there are  
687 several potential strategies. First, using transfer learning techniques can help adapt the  
688 model trained in one region to other regions with limited data. Integrating data from  
689 global observational networks (i.e., ARM) can also create a more diverse and  
690 representative training dataset, capturing a wider range of atmospheric conditions and  
691 cloud characteristics. Meanwhile, leveraging satellite data can provide broader  
692 coverage and enhance the robustness of the model. We plan to explore these approaches  
693 in future work to enhance the model's performance and applicability on a global scale.

694

695



696 **Code and data availability.** The code package of DNN models and for the simulation  
697 outputs of BLCs from observed meteorological data and ERA5 and MERRA-2 is  
698 available under the GNU General Public License v3.0 at  
699 <https://doi.org/10.5281/zenodo.10719342> (Su, 2024). ARM radiosonde data, surface  
700 fluxes, and cloud masks are available at  
701 [https://adc.arm.gov/discovery/#/results/instrument\\_class\\_code::armbe](https://adc.arm.gov/discovery/#/results/instrument_class_code::armbe) (ARM user  
702 facility, 1994). ARSCL (Active Remote Sensing of Clouds) can be found in  
703 [https://adc.arm.gov/discovery/#/results/instrument\\_class\\_code::arscl](https://adc.arm.gov/discovery/#/results/instrument_class_code::arscl) (ARM user  
704 facility, 1996). MERRA-2 reanalysis data can be downloaded obtained from  
705 [https://disc.gsfc.nasa.gov/datasets/M2T1NXRAD\\_5.12.4/summary?keywords%E2%80%89=%E2%80%89MERRA-2%20tavg1\\_2d\\_rad\\_Nx](https://disc.gsfc.nasa.gov/datasets/M2T1NXRAD_5.12.4/summary?keywords%E2%80%89=%E2%80%89MERRA-2%20tavg1_2d_rad_Nx) (GMAO, 2015). ERA5  
706 reanalysis data are obtained from  
707 [https://cds.climate.copernicus.eu/cdsapp#!/dataset/reanalysis-era5-pressure-](https://cds.climate.copernicus.eu/cdsapp#!/dataset/reanalysis-era5-pressure-levels?tab=form)  
708 [levels?tab=form](https://cds.climate.copernicus.eu/cdsapp#!/dataset/reanalysis-era5-pressure-levels?tab=form) (Hersbach et al. 2023).

710

711 **Author contributions.** TS designed this study and carried out the analysis and model  
712 training. TS and YZ interpreted the data and wrote the manuscript. YZ supervised the  
713 project.

714

715 **Competing interests.** The contact author has declared that neither they nor their co-  
716 authors have any competing interests.

717

718 **Acknowledgements.** Work at LLNL is performed under the auspices of the U.S. DOE  
719 by Lawrence Livermore National Laboratory under Contract DE-AC52-07NA27344.  
720 This research used resources of the National Energy Research Scientific Computing

721 Center (NERSC), a U.S. Department of Energy Office of Science User Facility located  
722 at Lawrence Berkeley National Laboratory, operated under Contract No. DE-AC02-  
723 05CH11231. We acknowledge the U.S. Department of Energy's ARM program for  
724 offering the comprehensive filed observations.

725

726 **Financial support.** This work has been supported by the DOE Atmospheric System  
727 Research (ASR) Science Focus Area (SFA) THREAD project (SCW1800).

728

## 729 **References**

- 730 Altmann, A., Toloși, L., Sander, O. and Lengauer, T.: Permutation importance: a  
731 corrected feature importance measure. *Bioinformatics*, 26(10), pp.1340-1347.,  
732 2010.
- 733 Atmospheric Radiation Measurement (ARM) user facility.: ARM Best Estimate Data  
734 Products (ARMBEATM). Southern Great Plains (SGP) Central Facility, Lamont,  
735 OK (C1). Compiled by C. Xiao and X. Shaocheng. [Dataset] ARM Data Center.  
736 Dataset accessed 2023-12-25 at <http://dx.doi.org/10.5439/1333748>., 1994.
- 737 Atmospheric Radiation Measurement (ARM) user facility.: Active Remote Sensing of  
738 CLouds (ARSCL1CLOTH). 2024-02-05 to 2024-02-13, Southern Great Plains  
739 (SGP) Central Facility, Lamont, OK (C1). Compiled by S. Giangrande, D. Wang,  
740 E. Clothiaux and P. Kollias. [Dataset] ARM Data Center. Dataset accessed 2023-  
741 12-25 at <http://dx.doi.org/10.5439/1996113>., 1996.
- 742 Battaglia, P.W., Hamrick, J.B., Bapst, V., Sanchez-Gonzalez, A., Zambaldi, V.,  
743 Malinowski, M., Tacchetti, A., Raposo, D., Santoro, A., Faulkner, R. and Gulcehre,  
744 C.: Relational inductive biases, deep learning, and graph networks. arXiv preprint  
745 arXiv:1806.01261., 2018.
- 746 Berg, L. K., and Kassianov, E.I.: Temporal variability of fair-weather cumulus statistics  
747 at the ACRF SGP site. *J. Climate*, 21(13), 3344–3358., 2008.
- 748 Betts, A.K.: Land - surface - atmosphere coupling in observations and models. *Journal*  
749 *of Advances in Modeling Earth Systems*, 1(3)., 2009.
- 750 Bogenschutz, P. A., Eldred, C., & Caldwell, P. M.: Horizontal resolution sensitivity of  
751 the Simple Convection-Permitting E3SM Atmosphere Model in a doubly-periodic  
752 configuration. *Journal of Advances in Modeling Earth Systems*, 15,  
753 e2022MS003466. <https://doi.org/10.1029/2022MS003466>, 2023.
- 754 Bretherton, C. S., Blossey, P. N., and Uchida, J.: Cloud droplet sedimentation,  
755 entrainment efficiency, and subtropical stratocumulus albedo. *Geophys. Res. Lett.*,

756 34(3), L03813., 2007.

757 Cadeddu, M. P., Turner, D. D., and Liljegren, J. C.: A neural network for real-time  
758 retrievals of PWV and LWP from Arctic millimeter-wave ground-based  
759 observations, *IEEE T. Geosci. Remote*, 47, 1887–1900., 2009.

760 Caldwell, P.M., Terai, C.R., Hillman, B., Keen, N.D., Bogenschutz, P., Lin, W.,  
761 Beydoun, H., Taylor, M., Bertagna, L., Bradley, A.M. and Clevenger, T.C.:  
762 Convection - permitting simulations with the E3SM global atmosphere model.  
763 *Journal of Advances in Modeling Earth Systems*, 13(11), p.e2021MS002544., 2021.

764 Chandra, A. S., Kollias, P., Giangrande, S. E., & Klein, S. A.: Long-term observations  
765 of the convective boundary layer using insect radar returns at the SGP ARM climate  
766 research facility. *Journal of climate*, 23(21), 5699-5714., 2010.

767 Chu, Y., Li, J., Li, C., Tan, W., Su, T., and Li, J.: Seasonal and diurnal variability of  
768 planetary boundary layer height in Beijing: Intercomparison between MPL and  
769 WRF results, *Atmos. Res.*, 227, 1–13, 2019.

770 Clayson, C.A. and Chen, A.: Sensitivity of a coupled single-column model in the tropics  
771 to treatment of the interfacial parameterizations. *Journal of climate*, 15(14),  
772 pp.1805-1831., 2002.

773 Clothiaux, E. E., Ackerman, T. P., Mace, G. G., Moran, K. P., Marchand, R. T., Miller,  
774 M. A., and Martner, B. E.: Objective determination of cloud heights and radar  
775 reflectivities using a combination of active remote sensors at the ARM CART sites.  
776 *J. Appl. Meteorol.*, 39(5), 645–665., 2000.

777 Clothiaux, E.E., Miller, M.A., Perez, R.C., Turner, D.D., Moran, K.P., Martner, B.E.,  
778 Ackerman, T.P., Mace, G.G., Marchand, R.T., Widener, K.B. and Rodriguez, D.J.:  
779 The ARM millimeter wave cloud radars (MMCRs) and the active remote sensing  
780 of clouds (ARSCL) value added product (VAP) (No. DOE/SC-ARM/VAP-002.1).  
781 DOE Office of Science Atmospheric Radiation Measurement (ARM) Program  
782 (United States)., 2001.

783 Cook, D. R.: Energy Balance Bowen Ratio (EBBR) instrument handbook, Technical  
784 Report Rep. DOE/SC-ARM/TR-037, U.S. Department of Energy., 2018.

785 Date, Y. and Kikuchi, J.: Application of a deep neural network to metabolomics studies  
786 and its performance in determining important variables. *Analytical chemistry*, 90(3),  
787 pp.1805-1810., 2018.

788 De Roode, S.R., Siebesma, A.P., Dal Gesso, S., Jonker, H.J., Schalkwijk, J. and Sival,  
789 J.: A mixed - layer model study of the stratocumulus response to changes in large -  
790 scale conditions. *Journal of Advances in Modeling Earth Systems*, 6(4), pp.1256-  
791 1270., 2014.

792 Fast, J. D., Berg, L. K., Alexander, L., Bell, D., D'Ambro, E., Hubbe, J., Kuang, C., Liu,  
793 J., Long, C., Matthews, A., and Mei, F.: Overview of the HI-SCALE field campaign:  
794 A new perspective on shallow convective clouds, *B. Am. Meteorol. Soc.*, 100, 821–  
795 840.: , 2019.

796 Gagne II, D. J., Haupt, S. E., Nychka, D. W., and Thompson, G.: Interpretable deep  
797 learning for spatial analysis of severe hailstorms, *Mon. Weather Rev.*, 147.: 2845,  
798 (2019)., 2827.

799 Gelaro, R., McCarty, W., Suárez, M.J., Todling, R., Molod, A., Takacs, L., Randles,

800 C.A., Darnenov, A., Bosilovich, M.G., Reichle, R. and Wargan, K.: The modern-  
801 era retrospective analysis for research and applications, version 2 (MERRA-2).  
802 Journal of climate, 30(14), pp.5419-5454., 2017.

803 Gentine, P., Pritchard, M., Rasp, S., Reinaudi, G. and Yacalis, G.: Could machine  
804 learning break the convection parameterization deadlock?. Geophysical Research  
805 Letters, 45(11), pp.5742-5751., 2018.

806 Global Modeling and Assimilation Office (GMAO.: MERRA-2 tavg1\_2d\_rad\_Nx:  
807 2d,1-Hourly,Time-Averaged,Single-Level,Assimilation,Radiation Diagnostics  
808 V5.12.4, Greenbelt, MD, USA [Dataset]. Goddard Earth Sciences Data and  
809 Information Services Center (GES DISC),  
810 <https://doi.org/10.5067/Q9QMY5PBNV1T.>, 2015.

811 Golaz, J.C., Larson, V.E. and Cotton, W.R.: A PDF-based model for boundary layer  
812 clouds. Part I: Method and model description. Journal of the atmospheric sciences,  
813 59(24), pp.3540-3551., 2002.

814 Guo, J., Su, T., Chen, D., Wang, J., Li, Z., Lv, Y., ... & Zhai, P.: Declining summertime  
815 local - scale precipitation frequency over China and the United States, 1981 - 2012:  
816 The disparate roles of aerosols. Geophysical Research Letters, 46(22), 13281-  
817 13289., 2019.

818 Guo, J., Su, T., Li, Z., Miao, Y., Li, J., Liu, H., Xu, H., Cribb, M., and Zhai, P.: Declining  
819 frequency of summertime local-scale precipitation over eastern China from 1970 to  
820 2010 and its potential link to aerosols, Geophys. Res. Lett., 44, 5700–5708, 2017.

821 Guo, J., Zhang, J., Shao, J., Chen, T., Bai, K., Sun, Y., Li, N., Wu, J., Li, R., Li, J. and  
822 Guo, Q.: A merged continental planetary boundary layer height dataset based on  
823 high-resolution radiosonde measurements, ERA5 reanalysis, and GLDAS. Earth  
824 System Science Data, 16(1), pp.1-14., 2024.

825 Gustafson, W.I., Vogelmann, A.M., Li, Z., Cheng, X., Dumas, K.K., Endo, S., Johnson,  
826 K.L., Krishna, B., Fairless, T. and Xiao, H.: The large-eddy simulation (LES)  
827 atmospheric radiation measurement (ARM) symbiotic simulation and observation  
828 (LASSO) activity for continental shallow convection. Bulletin of the American  
829 Meteorological Society, 101(4), pp.E462-E479., 2020.

830 Haynes, J.M., Noh, Y.J., Miller, S.D., Haynes, K.D., Ebert-Uphoff, I. and Heidinger, A.:  
831 Low cloud detection in multilayer scenes using satellite imagery with machine  
832 learning methods. Journal of Atmospheric and Oceanic Technology, 39(3), pp.319-  
833 334., 2022.

834 Hersbach, H., Bell, B., Berrisford, P., Biavati, G., Horányi, A., Muñoz Sabater, J.,  
835 Nicolas, J., Peubey, C., Radu, R., Rozum, I., Schepers, D., Simmons, A., Soci, C.,  
836 Dee, D., Thépaut, J-N.: ERA5 hourly data on pressure levels from 1940 to present.  
837 [Dataset] Copernicus Climate Change Service (C3S) Climate Data Store (CDS),  
838 DOI: 10.24381/cds.bd0915c6., 2023.

839 Hersbach, H., Bell, B., Berrisford, P., Hirahara, S., Horányi, A., Muñoz - Sabater, J.,  
840 Nicolas, J., Peubey, C., Radu, R., Schepers, D. and Simmons, A.: The ERA5 global  
841 reanalysis. Quarterly Journal of the Royal Meteorological Society, 146(730),  
842 pp.1999-2049., 2020.

843 Holdridge, D., Ritsche, M., Prell, J., and Coulter, R.: Balloon-borne sounding system

844 (SONDE) handbook, <https://www.arm.gov/capabilities/instruments/sonde.>, 2011.

845 Holzworth, G. C.: Estimates of mean maximum mixing depths in the contiguous United  
846 States, *Mon. Weather Rev.*, 92, 235–242, [https://doi.org/10.1175/1520-0493\(1964\)092<0235:eommmmd>2.3.co;2](https://doi.org/10.1175/1520-0493(1964)092<0235:eommmmd>2.3.co;2), 1964., 1175.

848 Klambauer, G., Unterthiner, T., Mayr, A., & Hochreiter, S.: Self-normalizing neural  
849 networks. *Advances in neural information processing systems*, 30., 2017.

850 Kollias, P., Bharadwaj, N., Clothiaux, E.E., Lamer, K., Oue, M., Hardin, J., Isom, B.,  
851 Lindenmaier, I., Matthews, A., Luke, E.P. and Giangrande, S.E.: The ARM radar  
852 network: At the leading edge of cloud and precipitation observations. *Bulletin of  
853 the American Meteorological Society*, 101(5), pp.E588-E607., 2020.

854 Kuma, P., McDonald, A.J., Morgenstern, O., Alexander, S.P., Cassano, J.J., Garrett, S.,  
855 Halla, J., Hartery, S., Harvey, M.J., Parsons, S. and Plank, G.: Evaluation of  
856 Southern Ocean cloud in the HadGEM3 general circulation model and MERRA-2  
857 reanalysis using ship-based observations. *Atmospheric Chemistry and Physics*,  
858 20(11), pp.6607-6630., 2020.

859 Lareau, N.P., Zhang, Y. and Klein, S.A.: Observed boundary layer controls on shallow  
860 cumulus at the ARM Southern Great Plains site. *Journal of the Atmospheric  
861 Sciences*, 75(7), pp.2235-2255., 2018.

862 Lee, J.M., Zhang, Y. and Klein, S.A.: The effect of land surface heterogeneity and  
863 background wind on shallow cumulus clouds and the transition to deeper  
864 convection. *Journal of the Atmospheric Sciences*, 76(2), pp.401-419., 2019.

865 Lilly, D.K.: Models of cloud-topped mixed layers under a strong inversion. *Q.J.R.  
866 Meteorol. Soc.*, 94: 292-309. <https://doi.org/10.1002/qj.49709440106>, 1968.

867 Lu, C., Liu, Y. and Niu, S.: Examination of turbulent entrainment - mixing mechanisms  
868 using a combined approach. *Journal of Geophysical Research: Atmospheres*,  
869 116(D20), 2011.

870 Lu, C., Niu, S., Liu, Y. and Vogelmann, A.M.: Empirical relationship between  
871 entrainment rate and microphysics in cumulus clouds. *Geophysical Research  
872 Letters*, 40(10), pp.2333-2338., 2013.

873 Luque, A., Carrasco, A., Martín, A. and de Las Heras, A.: The impact of class imbalance  
874 in classification performance metrics based on the binary confusion matrix. *Pattern  
875 Recognition*, 91, pp.216-231., 2019.

876 McGovern, A., Elmore, K. L., Gagne, D. J., Haupt, S. E., Karstens, C. D., Lagerquist,  
877 R., Smith, T., and Williams, J. K.: Using artificial intelligence to improve real-time  
878 decision-making for high-impact weather, *B. Am. Meteorol. Soc.*, 98.: 2090,  
879 (2017)., 2073.

880 Miao, H., Wang, X., Liu, Y. and Wu, G.: An evaluation of cloud vertical structure in  
881 three reanalyses against CloudSat/cloud - aerosol lidar and infrared pathfinder  
882 satellite observations. *Atmospheric Science Letters*, 20(7), p.e906., 2019.

883 Moeng, C.H., Cotton, W.R., Bretherton, C., Chlond, A., Khairoutdinov, M., Krueger,  
884 S., Lewellen, W.S., MacVean, M.K., Pasquier, J.R.M., Rand, H.A. and Siebesma,  
885 A.P.: Simulation of a stratocumulus-topped planetary boundary layer:  
886 Intercomparison among different numerical codes. *Bulletin of the American  
887 Meteorological Society*, 77(2), pp.261-278., 1996.

888 Molero, F., Barragán, R. and Artíñano, B.: Estimation of the atmospheric boundary  
889 layer height by means of machine learning techniques using ground-level  
890 meteorological data. *Atmospheric Research*, 279, p.106401., 2022.

891 Mooers, G., Pritchard, M., Beucler, T., Ott, J., Yacalis, G., Baldi, P. and Gentine, P.:  
892 Assessing the potential of deep learning for emulating cloud superparameterization  
893 in climate models with real - geography boundary conditions. *Journal of Advances  
894 in Modeling Earth Systems*, 13(5), p.e2020MS002385., 2021.

895 Morrison, H., van Lier - Walqui, M., Fridlind, A.M., Grabowski, W.W., Harrington,  
896 J.Y., Hoose, C., Korolev, A., Kumjian, M.R., Milbrandt, J.A., Pawlowska, H. and  
897 Posselt, D.J.: Confronting the challenge of modeling cloud and precipitation  
898 microphysics. *Journal of advances in modeling earth systems*, 12(8),  
899 p.e2019MS001689., 2020.

900 Nogherotto, R., Tompkins, A.M., Giuliani, G., Coppola, E. and Giorgi, F.: Numerical  
901 framework and performance of the new multiple-phase cloud microphysics scheme  
902 in RegCM4. 5: precipitation, cloud microphysics, and cloud radiative effects.  
903 *Geoscientific Model Development*, 9(7), pp.2533-2547., 2016.

904 O'Gorman, P.A. and Dwyer, J.G.: Using machine learning to parameterize moist  
905 convection: Potential for modeling of climate, climate change, and extreme events.  
906 *Journal of Advances in Modeling Earth Systems*, 10(10), pp.2548-2563., 2018.

907 Pal, S.R., Steinbrecht, W. and Carswell, A.I.: Automated method for lidar determination  
908 of cloud-base height and vertical extent. *Applied optics*, 31(10), pp.1488-1494.,  
909 1992.

910 Pelly, J.L. and Belcher, S.E.: A mixed-layer model of the well-mixed stratocumulus-  
911 topped boundary layer. *Boundary-layer meteorology*, 100, pp.171-187., 2001.

912 Poll, S., Shrestha, P. and Simmer, C.: Grid resolution dependency of land surface  
913 heterogeneity effects on boundary - layer structure. *Quarterly Journal of the Royal  
914 Meteorological Society*, 148(742), pp.141-158., 2022.

915 Prein, A.F., Langhans, W., Fossier, G., Ferrone, A., Ban, N., Goergen, K., Keller, M.,  
916 Tölle, M., Gutjahr, O., Feser, F. and Brisson, E.: A review on regional convection -  
917 permitting climate modeling: Demonstrations, prospects, and challenges. *Reviews  
918 of geophysics*, 53(2), pp.323-361, 2015.

919 Qian, Y., Guo, Z., Larson, V.E., Leung, L.R., Lin, W., Ma, P.L., Wan, H., Wang, H.,  
920 Xiao, H., Xie, S. and Yang, B.: Region and cloud regime dependence of parametric  
921 sensitivity in E3SM atmosphere model. *Climate Dynamics*, pp.1-17., 2023.

922 Raju, V.G., Lakshmi, K.P., Jain, V.M., Kalidindi, A. and Padma, V.: August. Study the  
923 influence of normalization/transformation process on the accuracy of supervised  
924 classification. In *2020 Third International Conference on Smart Systems and  
925 Inventive Technology (ICSSIT)* (pp. 729-735). IEEE., 2020.

926 Randles, C.A., Da Silva, A.M., Buchard, V., Colarco, P.R., Darmenov, A., Govindaraju,  
927 R., Smirnov, A., Holben, B., Ferrare, R., Hair, J. and Shinozuka, Y.: The MERRA-  
928 2 aerosol reanalysis, 1980 onward. Part I: System description and data assimilation  
929 evaluation. *Journal of climate*, 30(17), pp.6823-6850., 2017.

930 Randall, D. A., Khairoutdinov, M., Arakawa, A., and Grabowski, W.: Breaking the  
931 cloud parameterization deadlock, *Bull. Am. Meteorol. Soc.*, 84, 1547–1564,

932 <https://doi.org/10.1175/BAMS-84-11-1547>, 2003.

933 Rasp, S.: Coupled online learning as a way to tackle instabilities and biases in neural  
934 network parameterizations: general algorithms and Lorenz 96 case study (v1. 0).  
935 Geoscientific Model Development, 13(5), pp.2185-2196., 2020.

936 Rieck, M., Hohenegger, C. and van Heerwaarden, C.C.: The influence of land surface  
937 heterogeneities on cloud size development. Monthly Weather Review, 142(10),  
938 pp.3830-3846., 2014.

939 Ritsche, M.: ARM Surface Meteorology Systems Instrument Handbook. PNNL:  
940 Richland, WA, USA., 2011.

941 Romps, D.M.: Exact expression for the lifting condensation level. Journal of the  
942 Atmospheric Sciences, 74(12), pp.3891-3900., 2017.

943 Roldón-Henao, N., Su, T., & Li, Z.: Refining planetary boundary layer height retrievals  
944 from micropulse - lidar at multiple ARM sites around the world. Journal of  
945 Geophysical Research: Atmospheres, 129(13), e2023JD040207,  
946 <https://doi.org/10.1029/2023JD040207>, 2024.

947 Sakaguchi, K., Berg, L.K., Chen, J., Fast, J., Newsom, R., Tai, S.L., Yang, Z., Gustafson  
948 Jr, W.I., Gaudet, B.J., Huang, M. and Pekour, M.: Determining spatial scales of soil  
949 moisture—Cloud coupling pathways using semi - idealized simulations. Journal of  
950 Geophysical Research: Atmospheres, 127(2), p.e2021JD035282., 2022.

951 Salimans, T., & Kingma, D. P.: Weight normalization: A simple reparameterization to  
952 accelerate training of deep neural networks. Advances in neural information  
953 processing systems, 29., 2016.

954 Shamekh, S., Lamb, K. D., Huang, Y., & Gentine, P.: Implicit learning of convective  
955 organization explains precipitation stochasticity. Proceedings of the National  
956 Academy of Sciences, 120(20), e2216158120., 2023.

957 Sisterson, D. L., Peppler, R. A., Cress, T. S., Lamb, P. J., & Turner, D. D.: The ARM  
958 Southern Great Plains (SGP) Site. Meteorological Monographs, 57(1), 6.1-6.14.  
959 <https://doi.org/10.1175/AMSMONOGRAPHS-D-16-0004.1>, 2016.

960 Song, H., Lin, W., Lin, Y., Wolf, A. B., Donner, L. J., Del Genio, A. D., ... & Liu, Y.:  
961 Evaluation of cloud fraction simulated by seven SCMs against the ARM  
962 observations at the SGP site. Journal of climate, 27(17), 6698-6719., 2014.

963 Stull, R.B.: An Introduction to Boundary Layer Meteorology. Dordrecht: Springer  
964 Netherlands, 1988.

965 Su, T.: Codes and Package of Deep Learning Driven Simulations of Boundary Layer  
966 Cloud over the US Southern Great Plains [Dataset]. Zenodo.  
967 <https://doi.org/10.5281/zenodo.10685605>, 2024.

968 Su, T., & Zhang, Y.: Deep-learning-derived planetary boundary layer height from  
969 conventional meteorological measurements. Atmospheric Chemistry and Physics,  
970 24(11), 6477-6493., 2024.

971 Su, T., Li, Z., and Kahn, R.: A new method to retrieve the diurnal variability of planetary  
972 boundary layer height from lidar under different thermodynamic stability conditions,  
973 Remote Sens. Environ., 237, 111519, 2020.

974 Su, T., Zheng, Y., and Li, Z.: Methodology to determine the coupling of continental  
975 clouds with surface and boundary layer height under cloudy conditions from lidar

976 and meteorological data, *Atmos. Chem. Phys.*, 22, 1453–1466,  
977 <https://doi.org/10.5194/acp-22-1453-2022>, 2022.

978 Su, T., Li, Z., and Zheng, Y.: Cloud-Surface Coupling Alters the Morning Transition  
979 From Stable to Unstable Boundary Layer, *Geophys. Res. Lett.*, 50, e2022GL102256,  
980 <https://doi.org/10.1029/2022GL102256>, 2023.

981 Su, T., Li, Z., Zhang, Y., Zheng, Y., and Zhang, H.: Observation and Reanalysis Derived  
982 Relationships Between Cloud and Land Surface Fluxes Across Cumulus and  
983 Stratiform Coupling Over the Southern Great Plains, *Geophys. Res. Lett.*, 51,  
984 e2023GL108090, <https://doi.org/10.1029/2023GL108090>, 2024.

985 Tang, Q., Xie, S., Zhang, Y., Phillips, T. J., Santanello, J. A., Cook, D. R., Riihimaki, L.  
986 D., and Gaustad, K. L.: Heterogeneity in warm-season land-atmosphere coupling  
987 over the US Southern Great Plains, *J. Geophys. Res.-Atmos.*, 123.: 7882, (2018).,  
988 7867.

989 Tang, S., Xie, S., Zhang, M., Tang, Q., Zhang, Y., Klein, S. A., Cook, D. R., and Sullivan,  
990 R. C.: Differences in eddy - correlation and energy - balance surface turbulent heat  
991 flux measurements and their impacts on the large - scale forcing fields at the ARM  
992 SGP site. *J. Geophys. Res. Atmos.*, 124, 3301–3318,  
993 [doi.org/10.1029/2018JD029689](https://doi.org/10.1029/2018JD029689)., 2019.

994 Tao, C., Zhang, Y., Tang, Q., Ma, H.Y., Ghate, V.P., Tang, S., Xie, S. and Santanello,  
995 J.A.: Land–Atmosphere coupling at the US Southern Great Plains: A comparison  
996 on local convective regimes between ARM observations, reanalysis, and climate  
997 model simulations. *Journal of Hydrometeorology*, 22(2), pp.463–481., 2021.

998 Tao, C., Zhang, Y., Tang, S., Tang, Q., Ma, H.Y., Xie, S. and Zhang, M.: Regional  
999 moisture budget and land - atmosphere coupling over the US Southern Great Plains  
1000 inferred from the ARM long - term observations. *Journal of Geophysical Research:*  
1001 *Atmospheres*, 124(17-18), pp.10091-10108., 2019.

1002 Teixeira, J., and Hogan, T. F.: Boundary layer clouds in a global atmospheric model:  
1003 simple cloud cover parameterizations. *J. Climate*, 15(11), 1261–1276., 2002.

1004 Tian, J., Zhang, Y., Klein, S.A., Öktem, R. and Wang, L.: How does land cover and its  
1005 heterogeneity length scales affect the formation of summertime shallow cumulus  
1006 clouds in observations from the US Southern Great Plains?. *Geophysical Research*  
1007 *Letters*, 49(7), p.e2021GL097070., 2022.

1008 Tiedtke, M.: Representation of clouds in large-scale models. *Monthly Weather Review*,  
1009 121(11), 3040-3061., 1993.

1010 Vassallo, D., Krishnamurthy, R., and Fernando, H. J. S.: Decreasing wind speed  
1011 extrapolation error via domain-specific feature extraction and selection, *Wind Energ.*  
1012 *Sci.*, 5, 959–975, [https://doi.org/10.: wes-5-959-2020](https://doi.org/10.1002/wes.5-959-2020), (2020)., 5194.

1013 Wang, C., Platnick, S., Meyer, K., Zhang, Z. and Zhou, Y.: A machine-learning-based  
1014 cloud detection and thermodynamic-phase classification algorithm using passive  
1015 spectral observations. *Atmospheric Measurement Techniques*, 13(5), pp.2257-2277.,  
1016 2020.

1017 Wang, Y., Zheng, X., Dong, X., Xi, B. and Yung, Y.L.: Insights of warm-cloud biases  
1018 in Community Atmospheric Model 5 and 6 from the single-column modeling  
1019 framework and Aerosol and Cloud Experiments in the Eastern North Atlantic



1020 (ACE-ENA) observations. *Atmospheric Chemistry and Physics*, 23(15), pp.8591-  
1021 8605., 2023.

1022 Xiao, H., Berg, L.K. and Huang, M.: The impact of surface heterogeneities and land -  
1023 atmosphere interactions on shallow clouds over ARM SGP site. *Journal of*  
1024 *Advances in Modeling Earth Systems*, 10(6), pp.1220-1244., 2018.

1025 Xiao, H., Berg, L.K. and Huang, M.: The impact of surface heterogeneities and land -  
1026 atmosphere interactions on shallow clouds over ARM SGP site. *Journal of*  
1027 *Advances in Modeling Earth Systems*, 10(6), pp.1220-1244., 2018.

1028 Xie, S., McCoy, R. B., Klein, S. A., Cederwall, R. T., Wiscombe, W. J., Jensen, M. P.,  
1029 Johnson, K. L., Clothiaux, E. E., Gaustad, K. L., Long, C. N., and Mather, J. H.:  
1030 Clouds and more: ARM climate modeling best estimate data: a new data product  
1031 for climate studies. *Bull. Amer. Meteorol. Soc.*, 91(1), 13–20., 2010.

1032 Yang, Y., Zheng, X., Gao, Z., Wang, H., Wang, T., Li, Y., Lau, G.N. and Yim, S.H.:  
1033 Long - term trends of persistent synoptic circulation events in planetary boundary  
1034 layer and their relationships with haze pollution in winter half year over eastern  
1035 China. *Journal of Geophysical Research: Atmospheres*, 123(19), pp.10-991., 2018.

1036 Yeo, H., Kim, M.H., Son, S.W., Jeong, J.H., Yoon, J.H., Kim, B.M. and Kim, S.W.:  
1037 Arctic cloud properties and associated radiative effects in the three newer reanalysis  
1038 datasets (ERA5, MERRA-2, JRA-55): Discrepancies and possible causes.  
1039 *Atmospheric Research*, 270, p.106080., 2022.

1040 Zhang, L., Dong, X., Kennedy, A., Xi, B. and Li, Z.: Evaluation of NASA GISS post-  
1041 CMIP5 single column model simulated clouds and precipitation using ARM  
1042 Southern Great Plains observations. *Advances in Atmospheric Sciences*, 34,  
1043 pp.306-320., 2017.

1044 Zhang, T., Lin, W., Vogelmann, A.M., Zhang, M., Xie, S., Qin, Y. and Golaz, J.C.:  
1045 Improving convection trigger functions in deep convective parameterization  
1046 schemes using machine learning. *Journal of Advances in Modeling Earth Systems*,  
1047 13(5), p.e2020MS002365., 2021.

1048 Zhang, Y. and Klein, S.A.: Mechanisms affecting the transition from shallow to deep  
1049 convection over land: Inferences from observations of the diurnal cycle collected at  
1050 the ARM Southern Great Plains site. *Journal of the Atmospheric Sciences*, 67(9),  
1051 pp.2943-2959., 2010.

1052 Zhang, Y. and Klein, S.A.: Factors controlling the vertical extent of fair-weather  
1053 shallow cumulus clouds over land: Investigation of diurnal-cycle observations  
1054 collected at the ARM Southern Great Plains site. *Journal of the Atmospheric*  
1055 *Sciences*, 70(4), pp.1297-1315., 2013.

1056 Zhang, Y., B. Stevens, B. Medeiros, and M. Ghil.: Low-Cloud Fraction, Lower-  
1057 Tropospheric Stability, and Large-Scale Divergence. *J. Climate*, 22, 4827–4844,  
1058 [https://doi.org/10.1175/2009JCLI2891.1.](https://doi.org/10.1175/2009JCLI2891.1), 2009.

1059 Zhang, Y., Klein, S.A., Fan, J., Chandra, A.S., Kollias, P., Xie, S. and Tang, S.: Large-  
1060 eddy simulation of shallow cumulus over land: A composite case based on ARM  
1061 long-term observations at its Southern Great Plains site. *Journal of the Atmospheric*  
1062 *Sciences*, 74(10), pp.3229-3251., 2017.

1063 Zhang, Y., Stevens, B. and Ghil, M.: On the diurnal cycle and susceptibility to aerosol

1064 concentration in a stratocumulus-topped mixed layer. Q.J.R. Meteorol. Soc., 131:  
1065 1567-1583. <https://doi.org/10.1256/qj.04.103>, 2005.

1066 Zheng, X., Tao, C., Zhang, C., Xie, S., Zhang, Y., Xi, B. and Dong, X.: Assessment of  
1067 CMIP5 and CMIP6 AMIP simulated clouds and surface shortwave radiation using  
1068 ARM observations over different climate regions. *Journal of Climate*, 36(24),  
1069 pp.8475-8495., 2023.

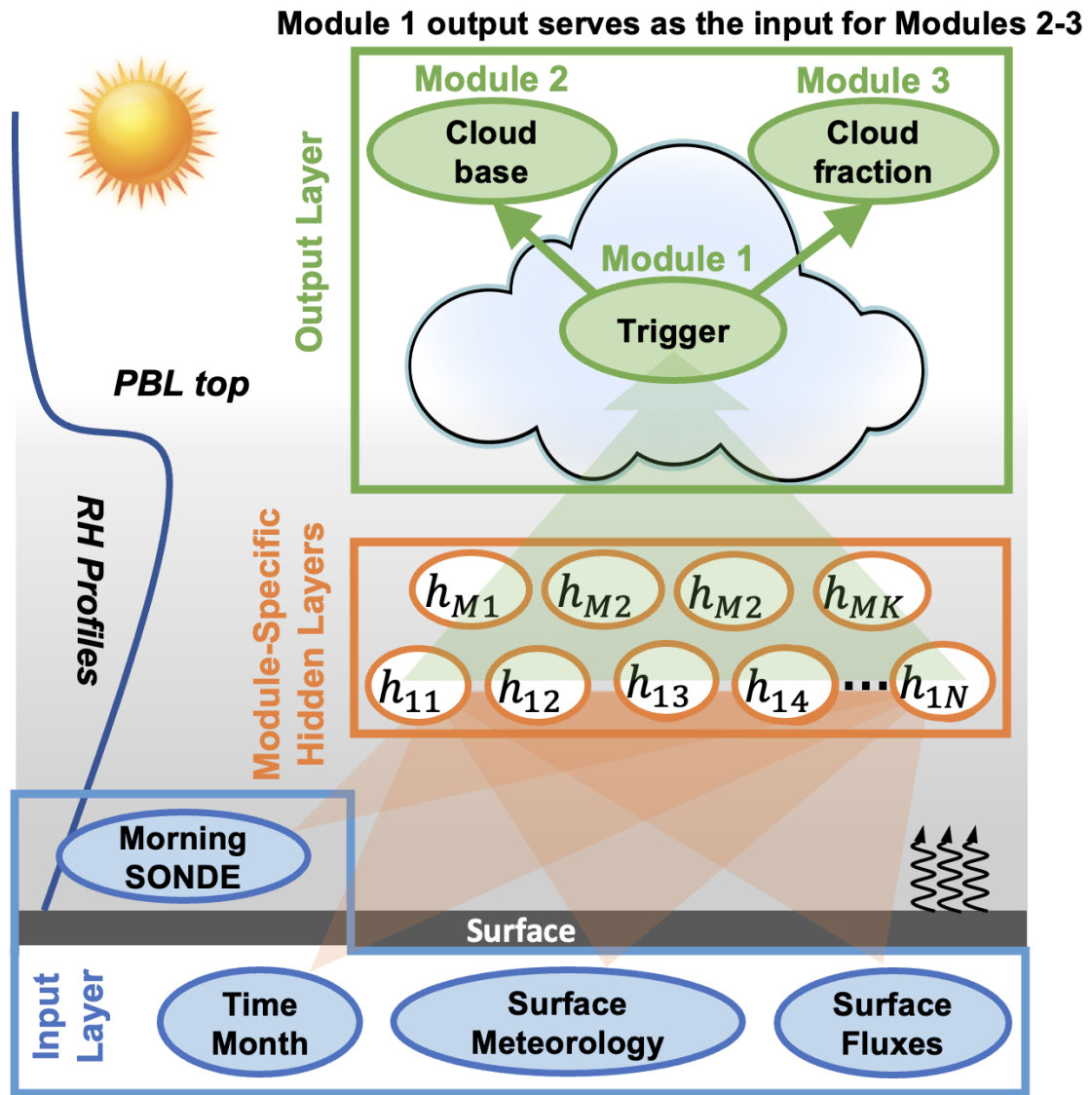
1070 Zheng, Y., Zhang, H., Rosenfeld, D., Lee, S. S., Su, T., & Li, Z.: Idealized large-eddy  
1071 simulations of stratocumulus advecting over cold water. Part I: Boundary layer  
1072 decoupling. *Journal of the Atmospheric Sciences*, 78(12), 4089-4102, 2021.

1073 **TABLE LIST:**

1074 **Table 1:** Detailed descriptions of input and output variables used in the deep learning  
 1075 models for predicting boundary layer clouds (BLCs). The table includes the variable  
 1076 names, descriptions, and data sources. For the input parameters, surface meteorology  
 1077 and fluxes are taken from the current and previous hours, while morning profiles  
 1078 comprises 46 values spanning from 0-8 km at 06 LT. Note that the output data is derived  
 1079 from ARSCL (Active Remote Sensing of Clouds). The three outputs correspond to the  
 1080 trigger module, cloud-base module, and fraction-thickness module, respectively.

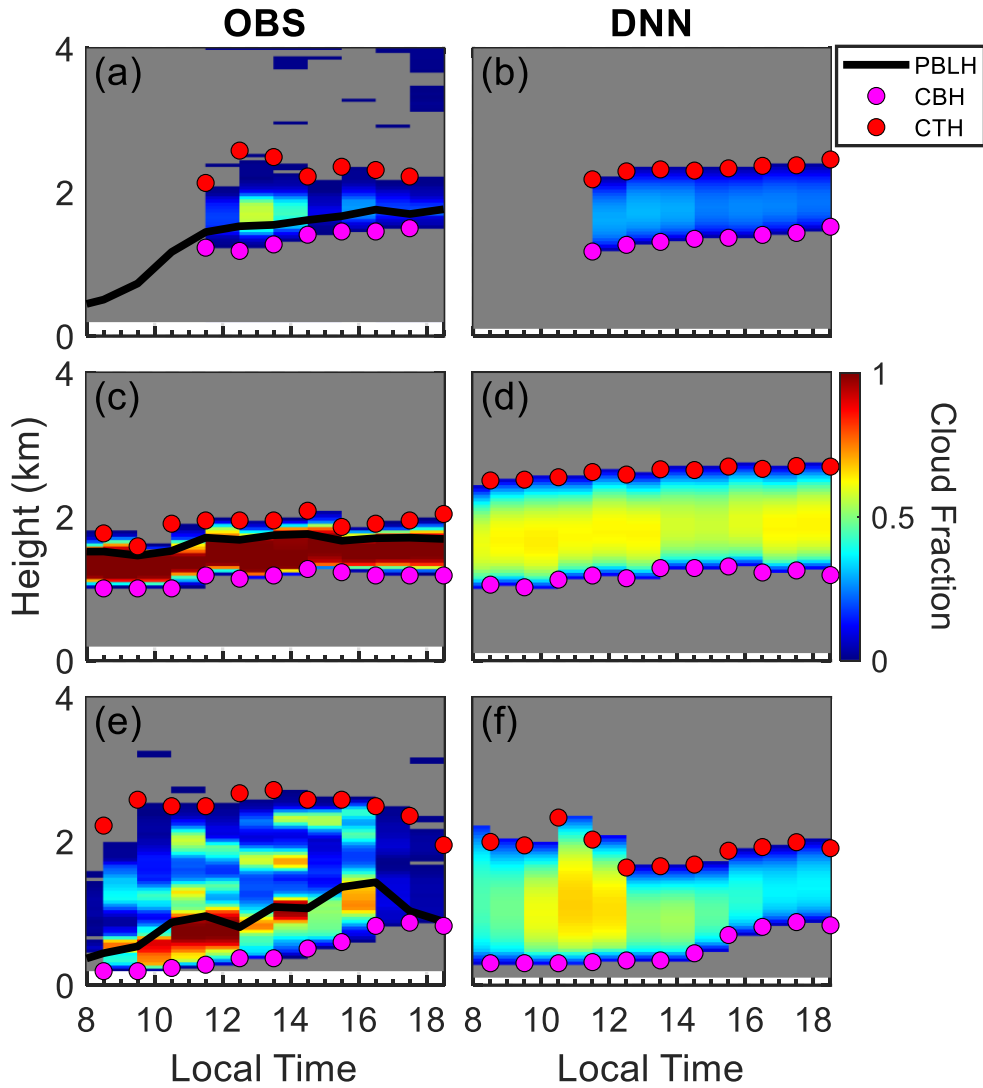
<b>Variable</b>	<b>Description</b>	<b>Data Source</b>
<b><i>Input</i></b>		
Month	Range from 1-12	Time Record
LT	Local Time	Time Record
PS	Pressure at surface level (2m)	Surface Meteorology Station
RH	Relative Humidity at 2m	Surface Meteorology Station
U	Zonal wind at 2m	Surface Meteorology Station
V	Meridional wind at 2m	Surface Meteorology Station
T	Temperature at 2m	Surface Meteorology Station
LCL	Lifted Condensation Level	Derived from T, RH, PS
SH	Sensible Heat	Energy Balance Bowen Ratio
LH	Latent Heat	Energy Balance Bowen Ratio
RH Profile	Morning RH profiles	Radiosonde
U Profile	Morning U wind profiles	Radiosonde
V Profile	Morning V wind profiles	Radiosonde
$\theta$ Profile	Morning potential temperature profiles	Radiosonde
BLH <sub>SH</sub>	PBLH derived from sensible heat	Derived from $\theta$ Profile and SH
BLH <sub>Parcel</sub>	PBLH derived from parcel method	Derived from $\theta$ Profile and T
<b><i>Output</i></b>		
Trigger	Cloud occurrence	ARSCL
Position	Cloud-base height	ARSCL
Fraction Profiles	Cloud fraction and thickness	ARSCL

1081  
 1082  
 1083  
 1084  
 1085  
 1086  
 1087  
 1088  
 1089  
 1090  
 1091  
 1092  
 1093



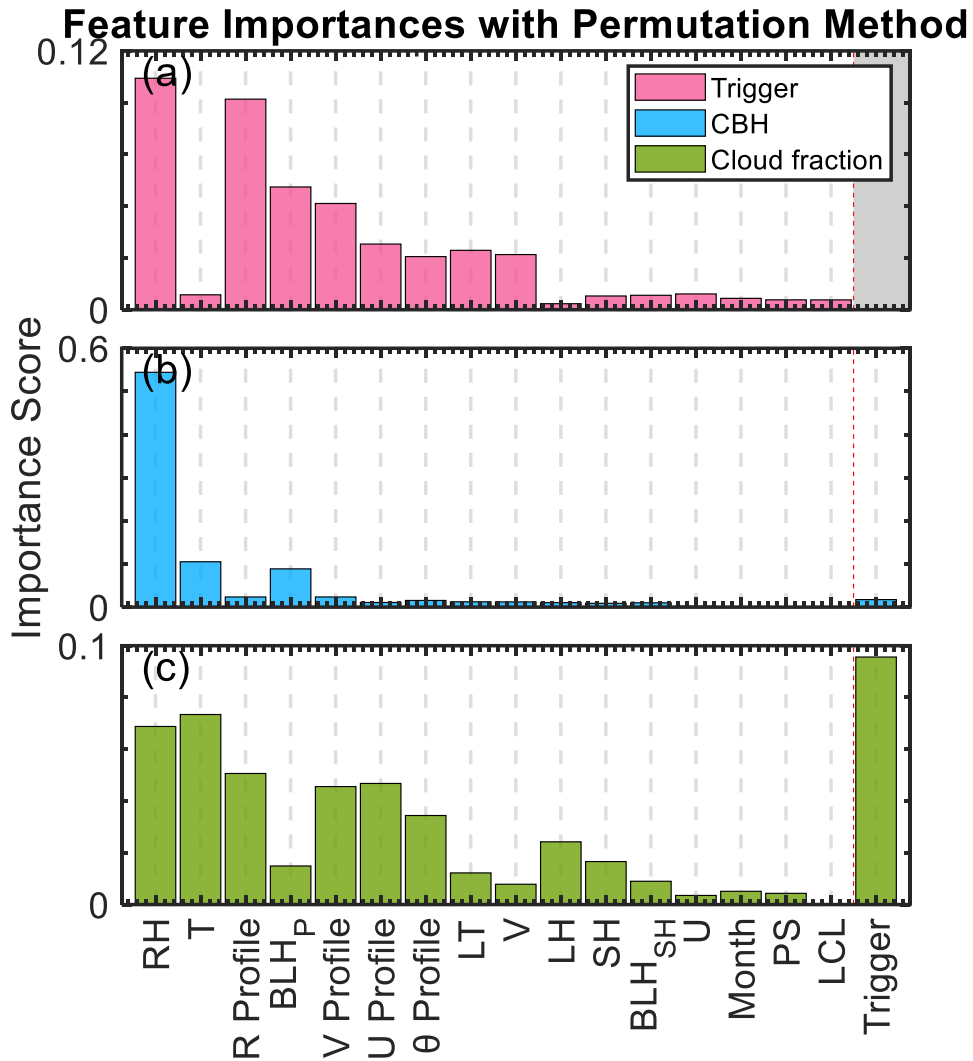
1095

1096 **Figure 1:** Conceptual diagram of the deep learning framework for simulating boundary  
 1097 layer cloud (BLC) characteristics over the US Southern Great Plains. Inputs for the deep  
 1098 neural networks (DNN) include morning meteorological profiles from radiosonde  
 1099 (SONDE), time indicators (i.e., local time and month), and surface conditions such as  
 1100 fluxes (curved black arrows) and meteorological data. The relevance of relative  
 1101 humidity (RH) profiles and the planetary boundary layer (PBL) top is emphasized due  
 1102 to their critical role in BLCs development. These variables are processed through  
 1103 multiple layers of hidden neurons ( $h_{11}$  to  $h_{MK}$ ). Both input and output parameters are  
 1104 hourly, except for the morning SONDE. Separate DNN modules are constructed for  
 1105 each task: Module 1 handles the initiation (trigger) of BLC; Module 2 estimates the  
 1106 cloud base; and Module 3 estimates cloud fraction and thickness. Together, these  
 1107 models synergize to predict the presence, altitude, and stratification of BLC.



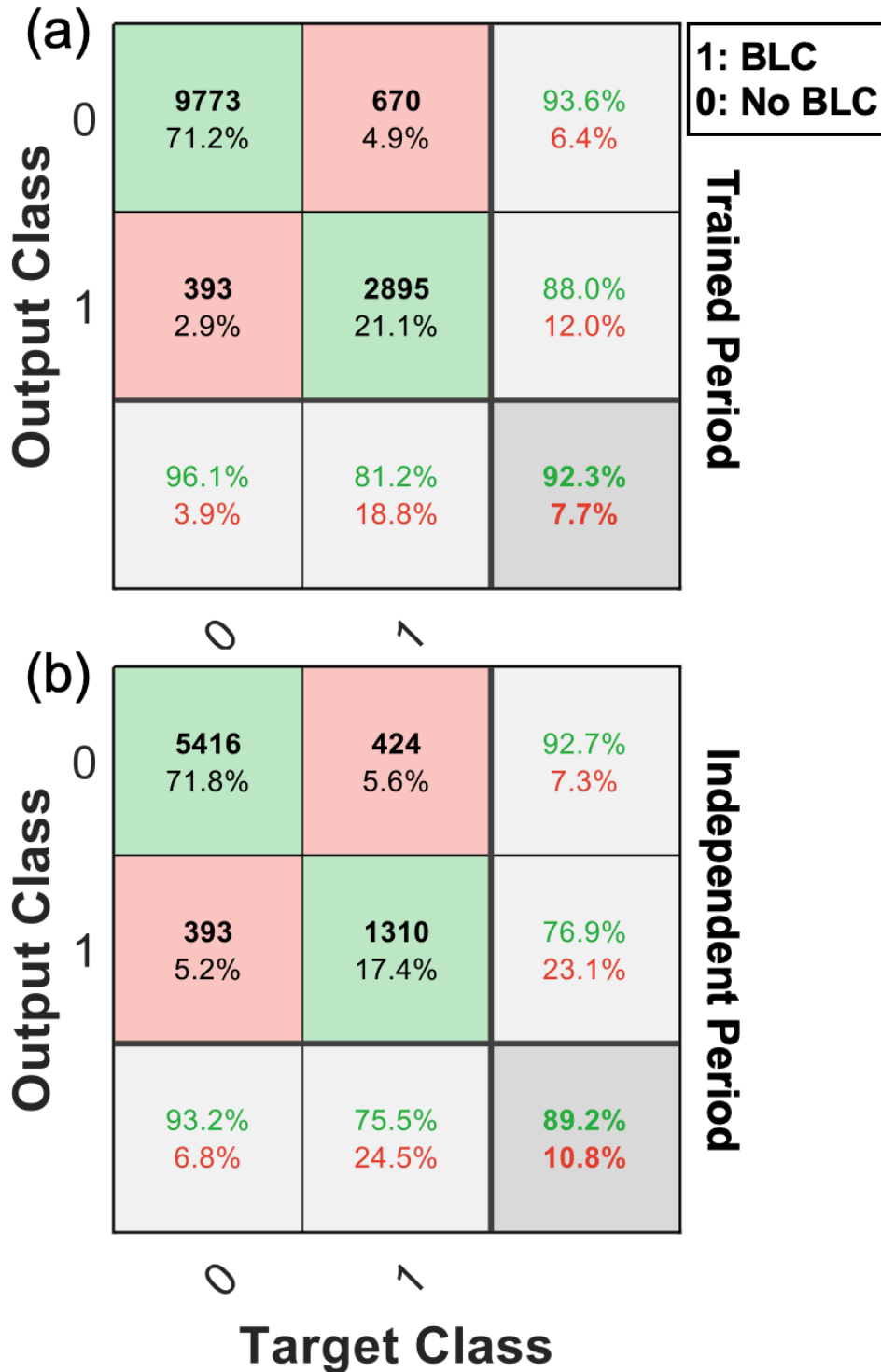
1108

1109 **Figure 2:** Examples of diurnal cloud fraction profiles for cumulus (a, b), stratiform (c,  
 1110 d), and complex cloud structures (e, f) over the US Southern Great Plains. Observed  
 1111 data (OBS) are shown alongside deep learning neural network (DNN) simulations.  
 1112 Black lines represent the observed PBL height (PBLH), with cloud base (CBH) and  
 1113 cloud top heights (CTH) marked by pink and red dots, respectively. The color gradient  
 1114 indicates the cloud fraction.



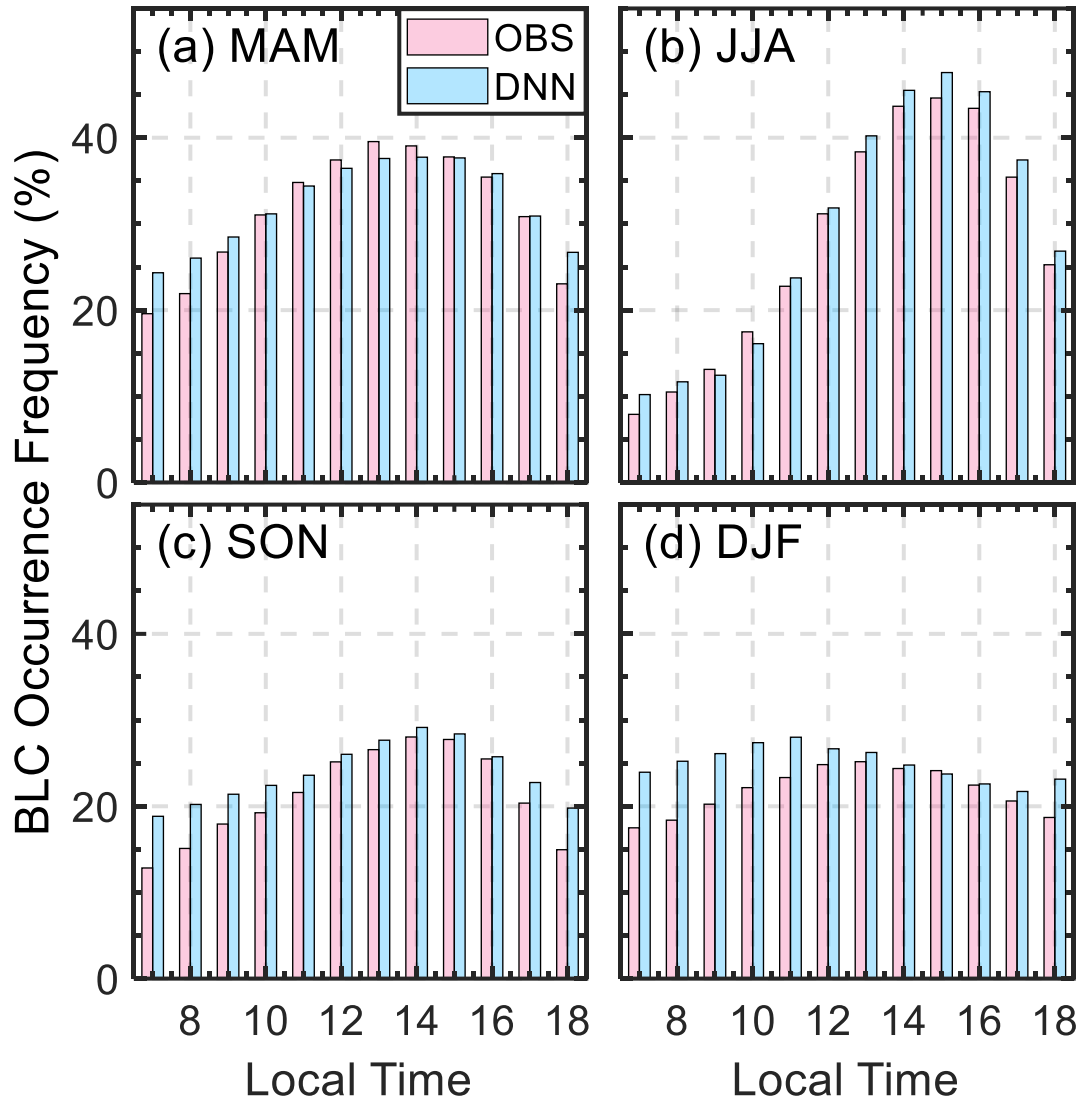
1115

1116 **Figure 3.** Feature importance scores for predicting cloud occurrence (a), cloud base  
 1117 height (CBH) (b), and cloud fraction (c) in the deep learning simulations of BLCs. Each  
 1118 panel presents the relative contribution of input features, includes month, local time  
 1119 (LT), surface pressure (PS), relative humidity (RH), zonal (U) and meridional (V) wind  
 1120 components, temperature (T), lifting condensation level (LCL), boundary layer height  
 1121 derived from sensible heat (BLH<sub>SH</sub>) and parcel methods (BLH<sub>Parcel</sub>), sensible heat (SH),  
 1122 latent heat (LH), and morning profiles of relative humidity (R Profile), U wind (U  
 1123 Profile), V wind (V Profile), and potential temperature ( $\theta$  Profile). These factors are  
 1124 ranked based on their overall importance. The importance scores are calculated with  
 1125 permutation method and quantify the relative contribution of each feature to the model's  
 1126 predictive accuracy.



1127

1128 **Figure 4:** Confusion matrices on the classification performance of the deep learning  
 1129 model in predicting the occurrence of boundary layer clouds (BLCs) during the trained  
 1130 period (1998-2016) in panel (a), and the independent period (2017-2020) in panel (b).  
 1131 The matrices in the trained period are calculated using the 30 % dataset for the  
 1132 validation. The matrices in the black color display the counts and percentages of true  
 1133 positive (TP), false positive (FP), true negative (TN), and false negative (FN)  
 1134 predictions. The overall accuracy, precision, and recall scores for each class are also  
 1135 included, demonstrating the model's ability in identifying BLC occurrence.



1136

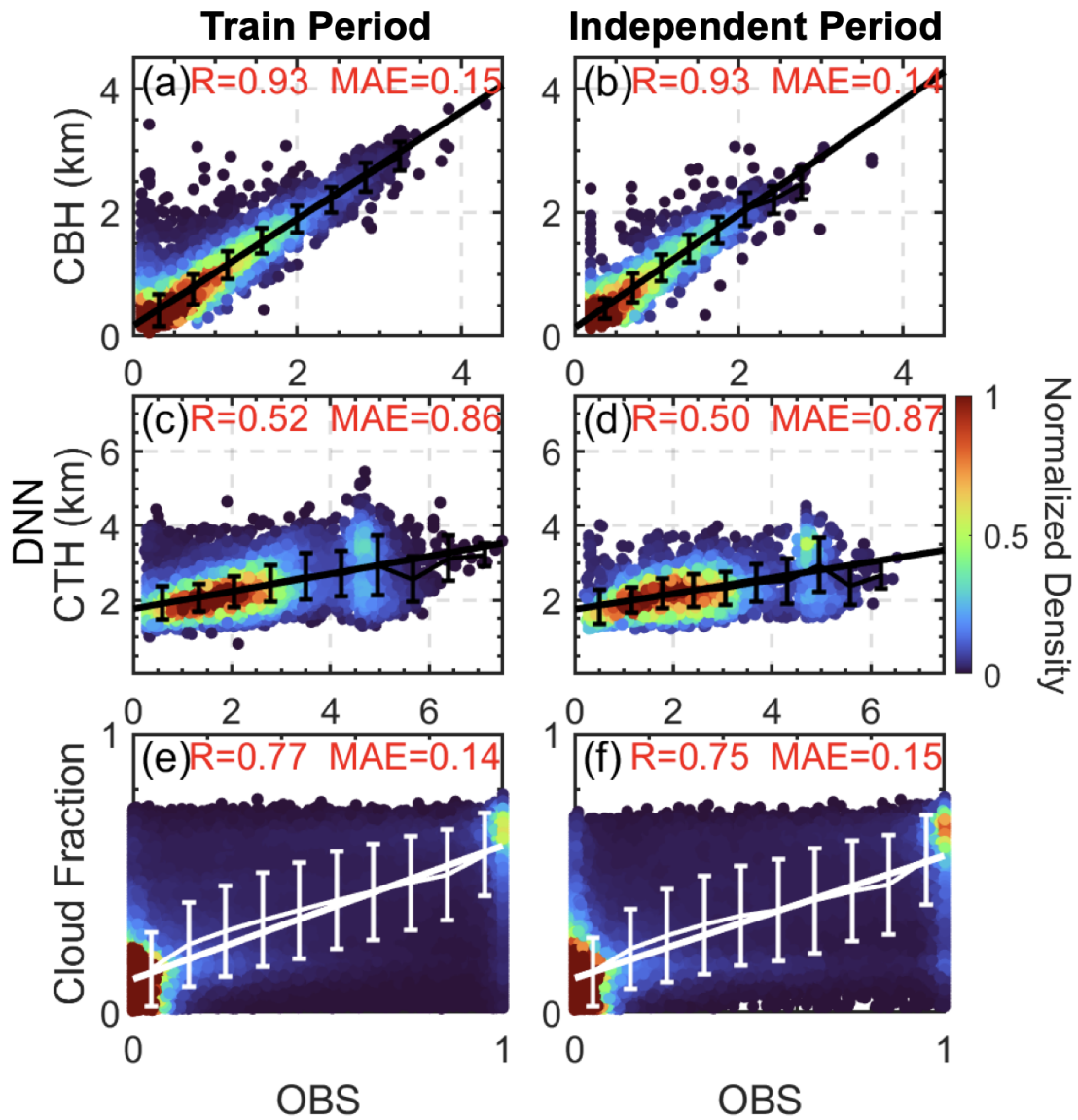
1137 **Figure 5.** Bar graph comparison on the occurrence frequency of boundary layer clouds  
 1138 (BLC) between the observed (OBS, red) and the predicted by the deep learning neural  
 1139 network (DNN, blue) across different local times of the day, segmented by seasons: (a)  
 1140 MAM (Spring), (b) JJA (Summer), (c) SON (Fall), and (d) DJF (Winter).

1141

1142

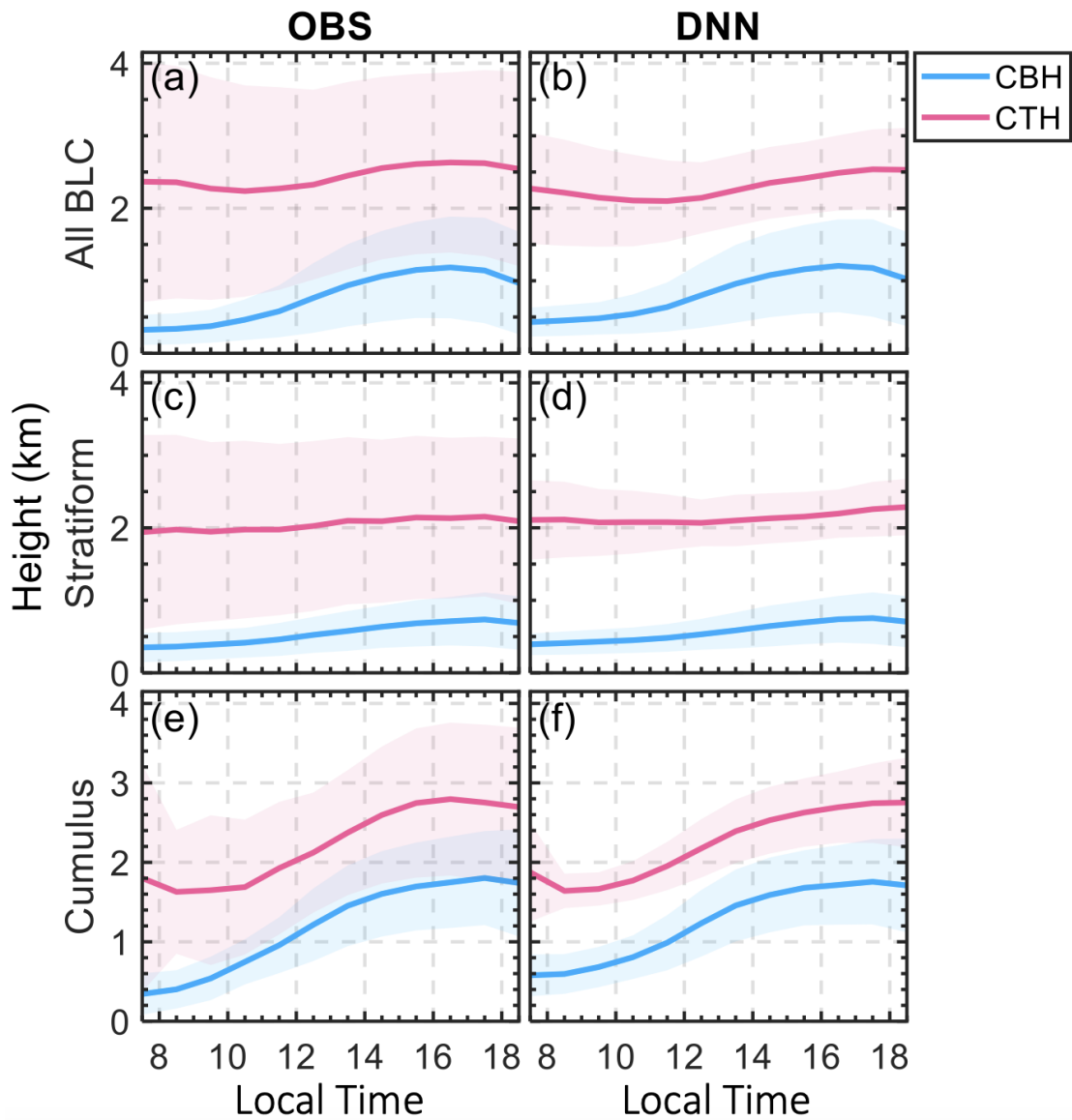
1143





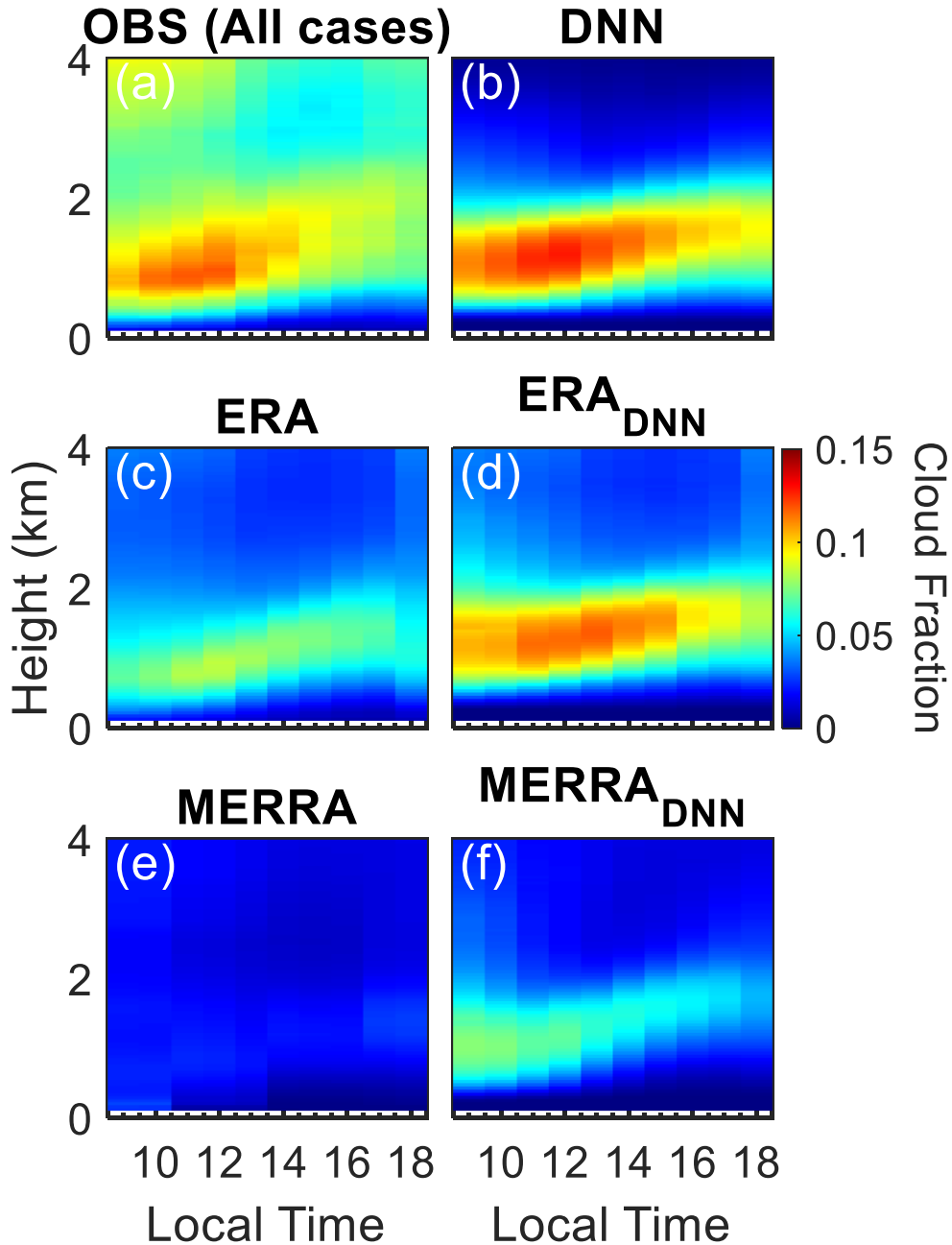
1144

1145 **Figure 6.** Scatter density comparison between the observed (OBS) and the predicted  
 1146 values by the deep learning neural network (DNN) for cloud base height (CBH), cloud  
 1147 top height (CTH), and cloud fraction during the trained period (a, c, e) and an  
 1148 independent period (b, d, f). Note that the BLC is segmented into ten layers, yielding  
 1149 ten separate cloud fraction values per BLC instance for analysis. The correlation  
 1150 coefficient (R) and mean absolute error (MAE) are indicated for each comparison. The  
 1151 color scale represents the normalized density of data points. The solid lines and error  
 1152 bars denoting the linear regression and standard deviations in each bar.



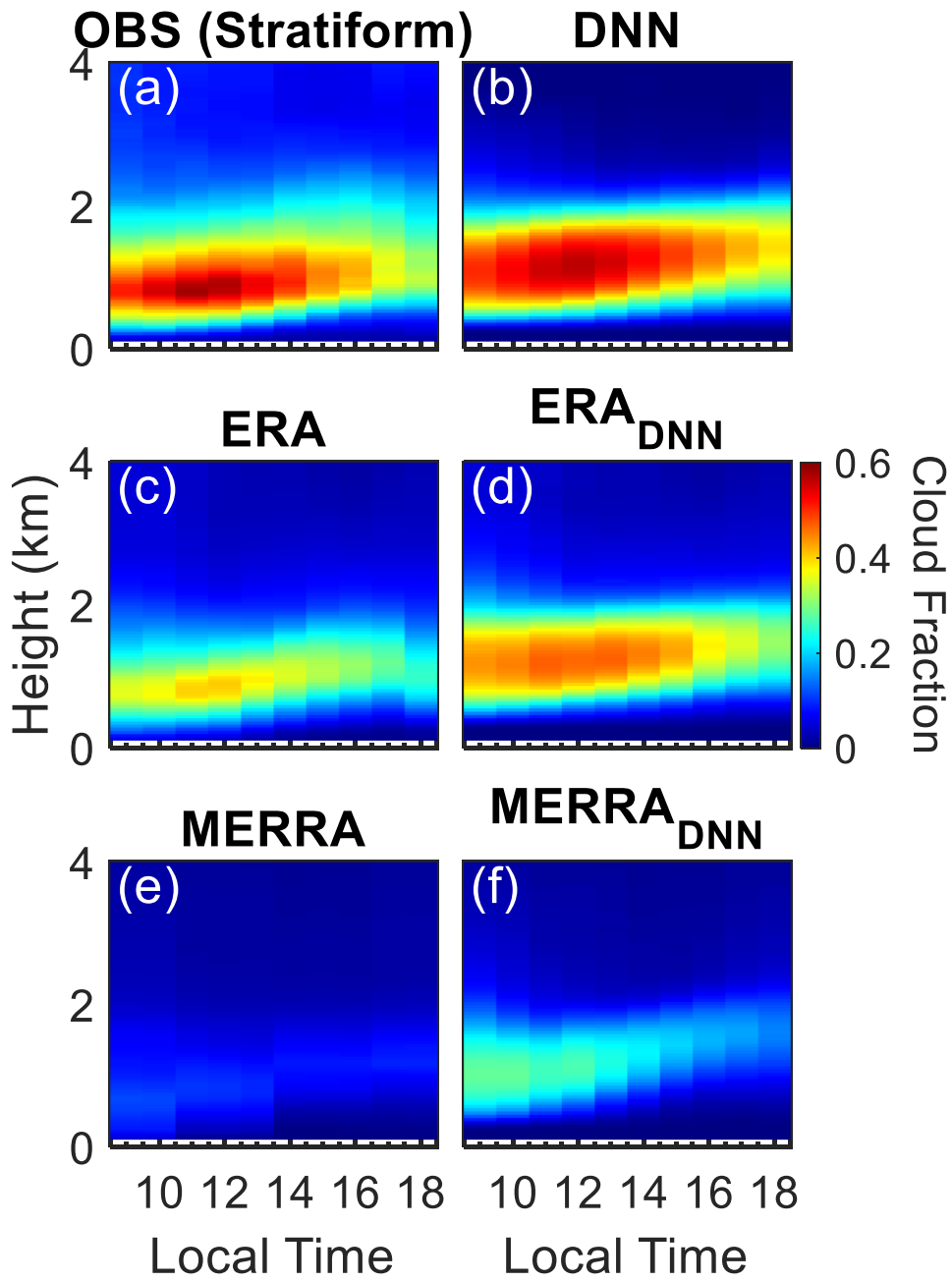
1153

1154 **Figure 7.** Diurnal profiles of cloud base height (CBH) and cloud top height (CTH) as  
 1155 determined by the observations (OBS) and deep learning simulations for all BLC (a-b),  
 1156 stratiform clouds (c-d), and cumulus (e-f). The shaded areas represent the variability  
 1157 (one standard deviation) around the mean heights.



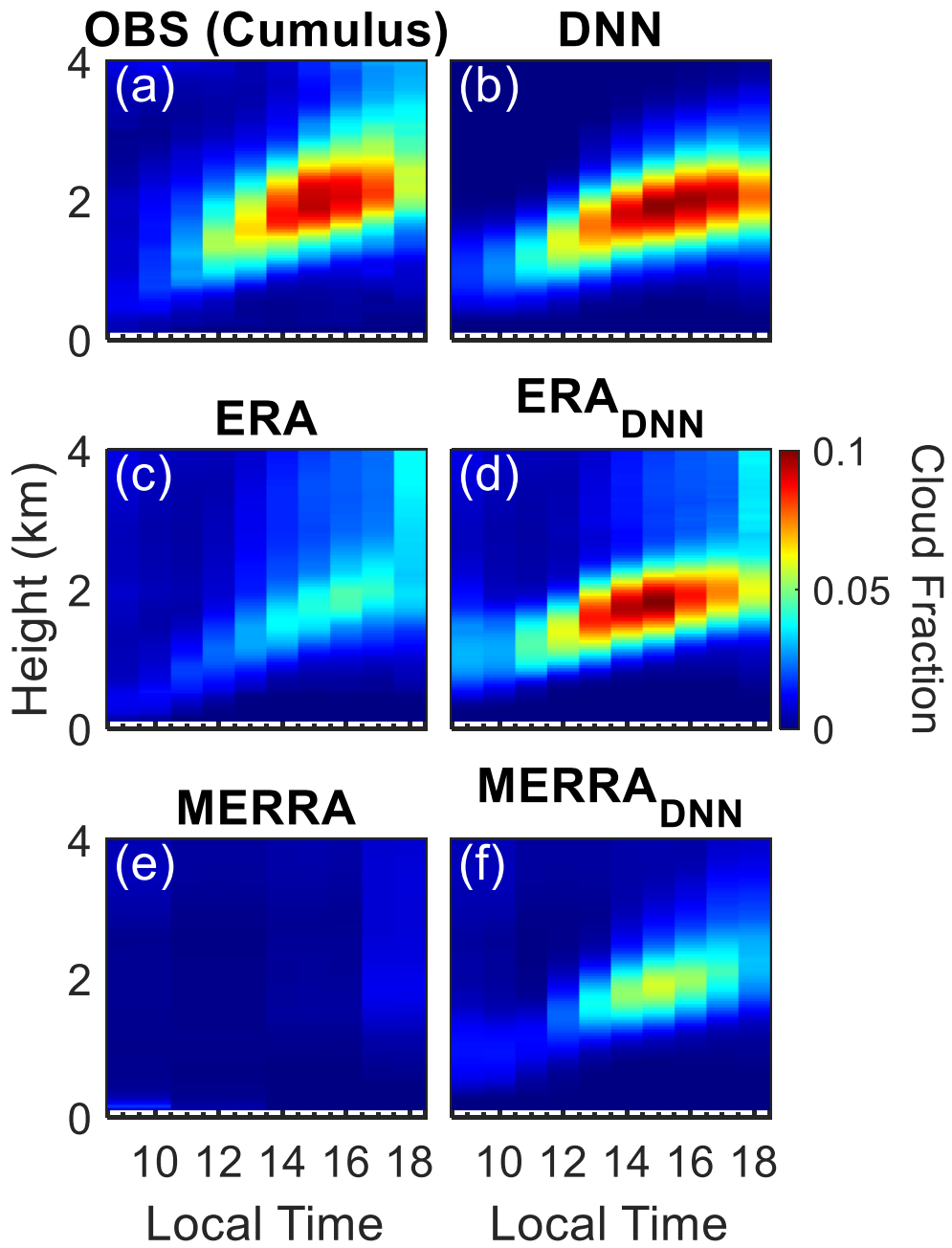
1158

1159 **Figure 8.** Color shaded areas demonstrate the diurnal variation in cloud fraction for all  
 1160 cases as observed and simulated. Panel (a) shows the observed cloud fraction (OBS),  
 1161 while panel (b) illustrates the cloud fraction simulated by the deep learning neural  
 1162 networks (DNN) using ARM observational data as inputs. (c, e): cloud fractions directly  
 1163 extracted from ERA and MERRA reanalysis datasets, respectively. (d, f): the cloud  
 1164 fractions simulated by the DNN model using ERA (ERA<sub>DNN</sub>) and MERRA  
 1165 (MERRA<sub>DNN</sub>) data as inputs.



1166

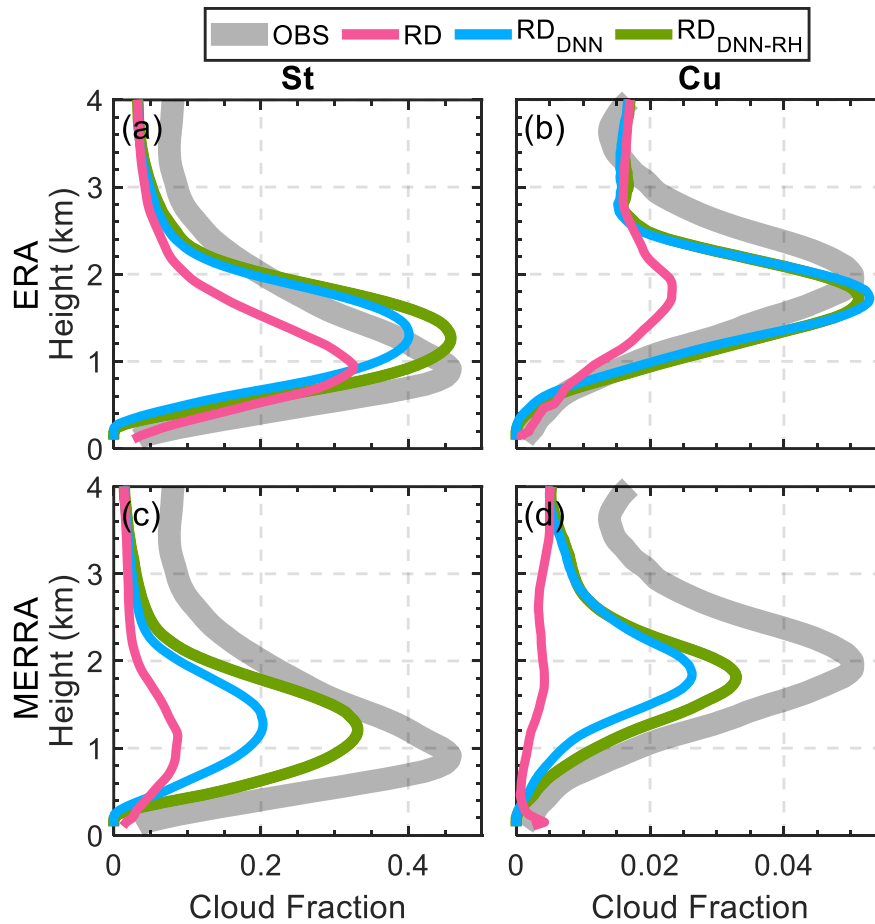
1167 **Figure 9.** Same to Figure 8, but for stratiform clouds.



1168

1169 **Figure 10.** Same to Figure 8, but for cumulus.

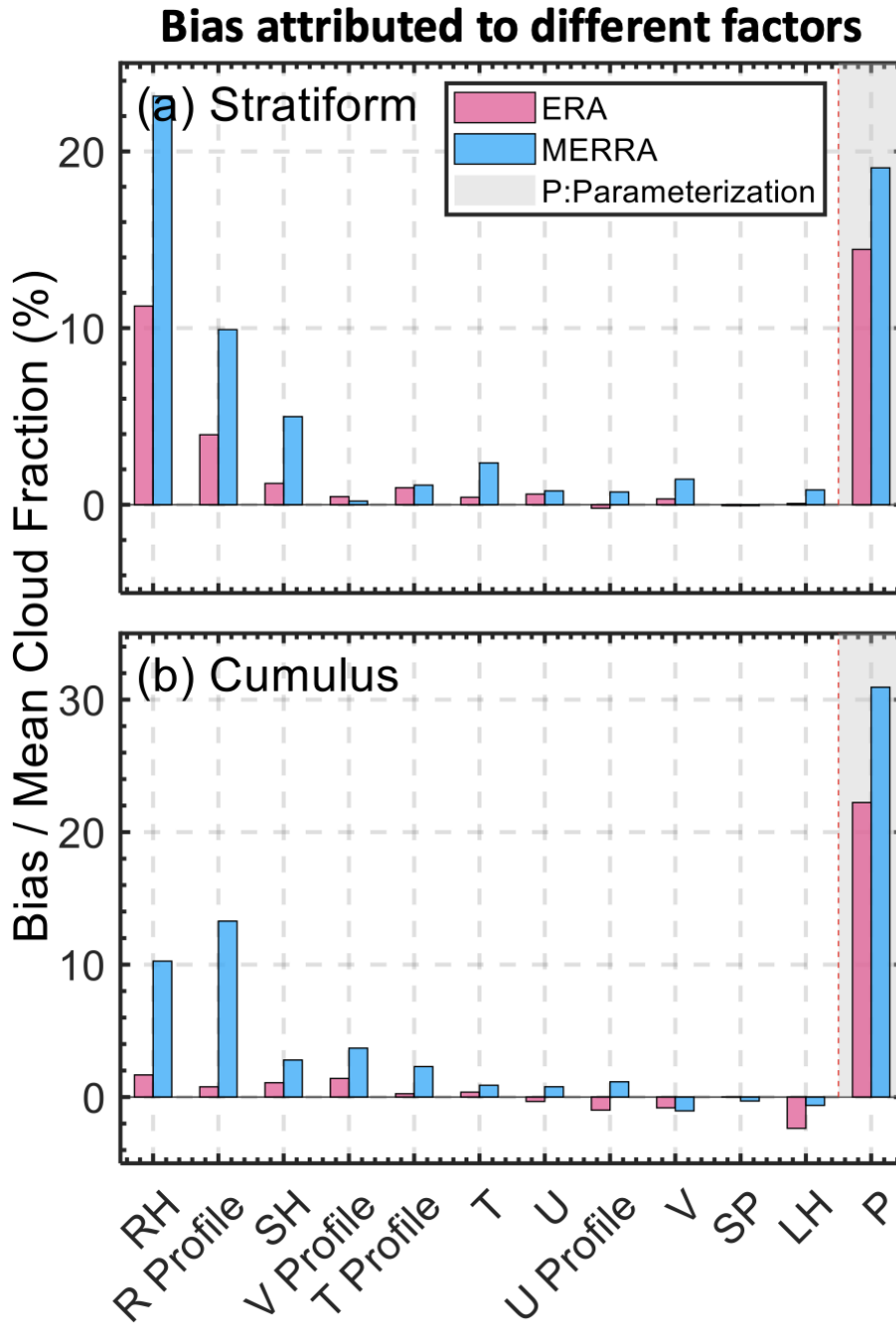
1170



1171

1172

1173 **Figure 11:** Vertical profiles of cloud fraction for stratiform (St) and cumulus (Cu)  
 1174 scenarios over the US Southern Great Plains. Panels (a) and (b) display ERA reanalysis  
 1175 data comparisons, while panels (c) and (d) show MERRA reanalysis data comparisons.  
 1176 The observed cloud fractions (OBS) are represented by the shaded grey area, illustrating  
 1177 the averaged cloud coverage recorded by field observations. The original reanalysis  
 1178 data (RD) is indicated in pink, indicating the baseline cloud fraction profiles as  
 1179 simulated by the reanalysis. The  $RD_{DNN}$  profiles in blue depict the new simulation  
 1180 results after applying the DNN models to the reanalysis data for boundary layer cloud  
 1181 (BLC) simulation. The  $RD_{DNN-RH}$  profiles in green show the simulation results when  
 1182 the surface relative humidity (RH) from the reanalysis data is replaced with observed  
 1183 values, indicating the impact of accurate surface moisture representation on cloud  
 1184 fraction simulations.



1185

1186 **Figure 12:** Attribution of bias between observed and reanalysis on cloud fractions to  
 1187 various meteorological factors and parameterization schemes for stratiform (a) and  
 1188 cumulus (b) cloud scenarios. The bars represent the normalized bias (bias divide mean  
 1189 cloud fraction) contributed by each factor: relative humidity profile (RH), meridional  
 1190 wind profile (V Profile), temperature profile (T Profile), zonal wind profile (U Profile),  
 1191 surface pressure (SP), latent heat flux (LH), and parameterization (P). All profiles took  
 1192 on morning (06:00 LT). Light blue bars indicate biases identified in the ERA reanalysis  
 1193 dataset, while pink bars represent biases in the MERRA reanalysis dataset. The dashed  
 1194 red line marked 'P' denotes biases attributed specifically to the parameterization within  
 1195 the reanalysis models. This analysis uses the DNN to discern the impact of each factor  
 1196 (ranked from highest to lowest) on the discrepancy in cloud fraction estimates between  
 1197 observations and reanalysis models.